Chemical Geology 622 (2023) 121347

Contents lists available at ScienceDirect

Chemical Geology

journal homepage: www.elsevier.com/locate/chemgeo

Stable Sn isotope signatures of Mid-ocean ridge basalts

Jia-Xin She [a,b,c], Edith Kubik [c], Weiqiang Li [a,b,*], Frédéric Moynier [c]

[a] State Key Laboratory for Mineral Deposits Research, School of Earth Sciences and Engineering, Nanjing University, Nanjing, Jiangsu 210023, China
[b] Frontiers Science Center for Critical Earth Material Cycling, Nanjing University, Nanjing, China
[c] Université Paris Cité, Institut de Physique du Globe de Paris, CNRS, UMR 7154, F-75005 Paris, France

ARTICLE INFO

Editor: Don Porcelli

Keywords:
Sn isotope
MORB
Magmatic differentiation
DMM
Oceanic crust

ABSTRACT

The constraint of Sn isotope composition of the Earth's mantle is the prerequisite for understanding planet formation with Sn isotopes and Sn isotope fractionation in terrestrial reservoirs. However, previous estimates of the Sn isotope composition of the Earth's mantle are hampered by the small number of mantle-related samples. In this study, we analyzed Sn stable isotope compositions of 27 basalts from geochemically and geologically diverse mid-ocean ridge segments, to constrain the Sn isotope composition of the depleted mantle source. The spread of Sn isotope compositions for the 27 different mid-ocean ridge basalts (MORBs) is limited, with $\delta^{122/118}Sn_{BHVO\text{-}2}$ (delta notation of $^{122}Sn/^{118}Sn$ ratios relative to USGS BHVO-2 basalt standard) values ranging from -0.051 ± 0.015‰ to 0.209 ± 0.016‰ ($\delta^{122/118}Sn_{3161a}$ from 0.280 ± 0.015 to 0.540 ± 0.016‰), despite great geochemical and geographical diversities of the samples. The slightly higher $\delta^{122/118}Sn_{BHVO\text{-}2}$ value (up to 0.209 ± 0.016‰ ($\delta^{122/118}Sn_{3161a}$ up to 0.540 ± 0.016‰)) of one MORB sample appears to be caused by post-eruptive alteration of the basalts. Other than that, the $\delta^{122/118}Sn_{BHVO\text{-}2}$ values of the MORB samples do not show correlations with sample latitude, spreading rate of mid-ocean ridge, MgO content of the bulk rock samples, and partial melting index $Na_{8.0}$ (defined as $[Na_2O] + 0.373 \times [MgO] - 2.98$), implying that Sn isotopes do not fractionate significantly during MORB melt generation and evolution processes. This study confirms the limited Sn isotopic variability between fresh MORBs globally, pointing to the Sn isotopic homogeneity of the depleted mantle source. Using these new MORB data, we proposed an estimate of the $\delta^{122/118}Sn_{BHVO\text{-}2}$ value for the Earth's depleted mantle to be 0.036 ± 0.087‰ ($\delta^{122/118}Sn_{3161a}$ of 0.367 ± 0.087‰) (2SD, $N = 12$). This value provides a reference point for understanding the planetary and magmatic processes of Earth from a Sn isotope perspective.

1. Introduction

Tin has the largest number of stable isotopes and the widest isotope mass range in the periodic table. The mass-dependent Sn isotope compositions are variable between different types of chondrites, which have been used to constrain the nature of the building blocks for the proto-Earth (Creech and Moynier, 2019; Wang et al., 2021b). Tin is a moderately volatile element with a 50% condensation temperature of 604 K (Wood et al., 2019). The elemental abundance and isotopic composition of Sn in planetary bodies are affected by volatilization-condensation processes that occurred during the early stages of planet formation and evolution, thus its isotopic composition can provide unique insights into planetary processes (Creech and Moynier, 2019; Wang et al., 2019a; Wang et al., 2021b), complementing with those of other elements of different volatility. For example, the lunar rocks have heavier isotopic compositions compared to terrestrial rocks and primitive meteorites (Day and Moynier, 2014) for a wide range of volatile elements, including Cl (Barnes et al., 2016; McCubbin et al., 2015; Sharp et al., 2010), Rb (Pringle and Moynier, 2017), Ga (Kato and Moynier, 2017), K (Wang and Jacobsen, 2016), Zn (Gargano et al., 2022; Kato et al., 2015; Paniello et al., 2012), but with an exception for Sn. Tin, an element with volatility within the range of the above elements, shows a reverse isotopic effect with the lunar rocks enriched in light Sn isotopes relative to mantle-derived rocks from Earth (Wang et al., 2019a). The unusual isotopic signatures of Sn for the Earth-Moon system led to a proposal of specific Sn speciation and condensing conditions in the protolunar disk (Wang et al., 2019a). Nonetheless, our understanding of the Sn isotope signatures of the Earth-Moon system is limited by the

* Corresponding author at: State Key Laboratory for Mineral Deposits Research, School of Earth Sciences and Engineering, Nanjing University, Nanjing, Jiangsu 210023, China.
E-mail address: liweiqiang@nju.edu.cn (W. Li).

https://doi.org/10.1016/j.chemgeo.2023.121347
Received 19 September 2022; Received in revised form 28 December 2022; Accepted 22 January 2023
Available online 26 January 2023

estimate of Earth's mantle Sn isotopic baseline, which is based on a very limited number of samples (komatiite, OIB, peridotite, MORB) (Badullovich et al., 2017; Wang et al., 2018).

Applications of Sn isotopes in planetary studies require a precise and accurate estimate of the Sn isotope composition of the bulk Earth. Geochemically, Sn exhibits lithophile, siderophile, and chalcophile behaviors (Badullovich et al., 2017; Witt-Eickschen et al., 2009; Yi et al., 1995). Tin is moderately incompatible during mantle melting (Adam and Green, 2006; Kamenetsky and Eggins, 2012; Michely et al., 2017) but can still be hosted by minerals like sulfides, clinopyroxene, titanite, amphibole, garnet, and mica (Che et al., 2013; Wang et al., 2018; Witt-Eickschen et al., 2009; Yi et al., 1995). The Sn concentration of the primitive mantle was estimated to be between 0.12 and 0.17 μg/g (Jochum et al., 1993; Sun and McDonough, 1989), whereas Sn is significantly enriched in crustal rocks (Sn ~1.7 μg/g in the bulk crust) (Rudnick and Gao, 2003). It is estimated that the crust accounts for only 5.1% of the bulk silicate Earth (BSE) Sn budget (Huang et al., 2013; Rudnick and Gao, 2003; Sun and McDonough, 1989). A part of the Earth Sn budget could reside in the Earth's core due to its affinity for metallic core, which is much less accessible. Therefore, the mantle is the key to

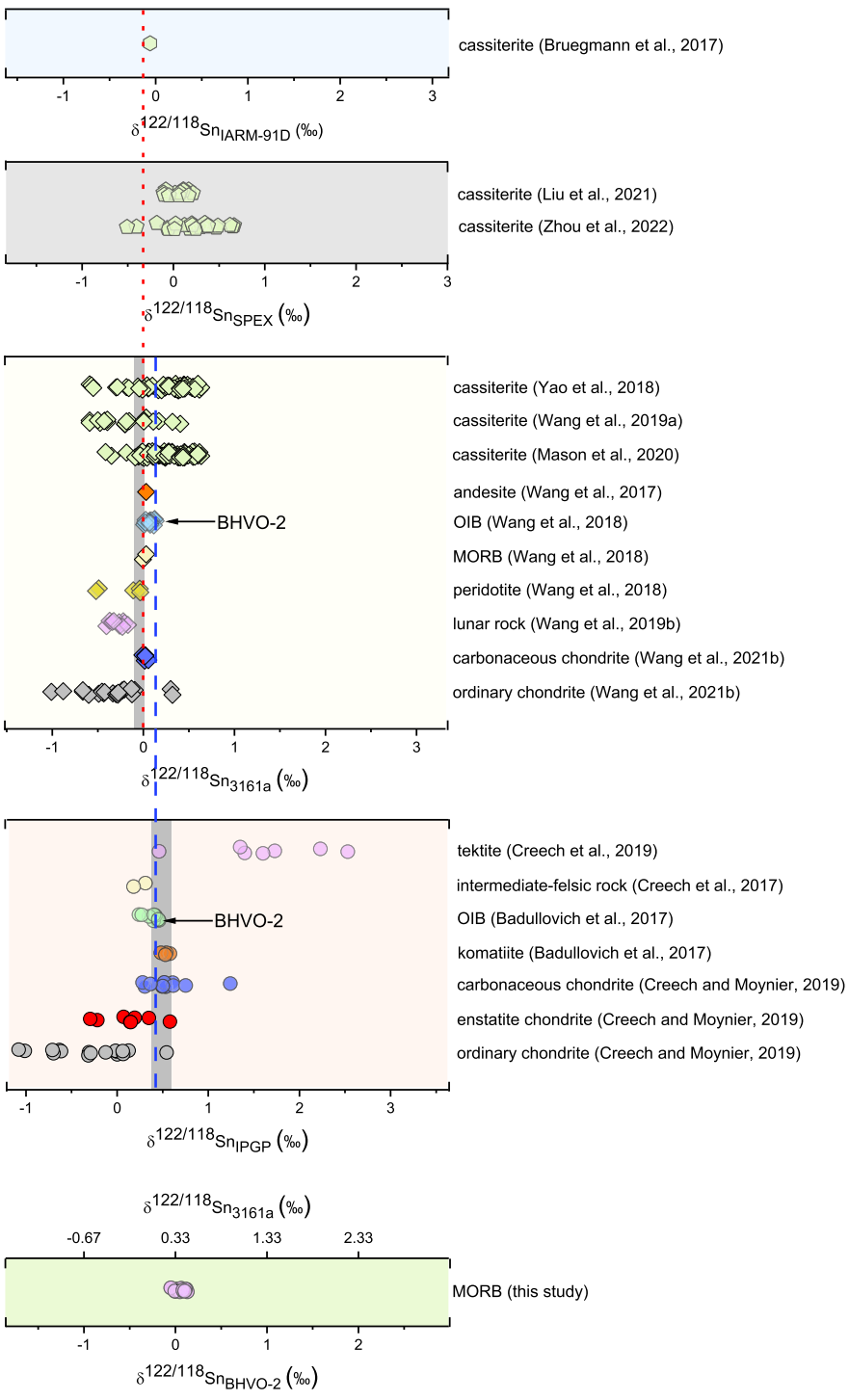

Fig. 1. Compilation of Sn isotope data of rocks, chondrites, and cassiterites. The data using IPGP as the standard are from Badullovich et al. (2017), Creech et al. (2017); Creech et al. (2019); Creech and Moynier (2019); the data using NIST as the standard from Mason et al. (2020); Wang et al. (2019b); Wang et al. (2018); Wang et al. (2017); Wang et al. (2019a); Wang et al. (2021a); Yao et al. (2018); data using SPEX as the standard is from Liu et al. (2021a); Zhou et al. (2022); data with IARM-91D is from Bruegmann et al. (2017). The data of this study are also displayed. The red dotted line represents the reference line for the NIST 3161a standard, whereas the blue dashed line represents the value for BHVO-2, assuming the two standards are isotopically identical between different laboratories. The shaded areas denote the estimated value range for BSE from Badullovich et al. (2017) and Wang et al. (2018), respectively. (For interpretation of the references to colour in this figure legend, the reader is referred to the web version of this article.)

the estimation of the Sn isotope composition of the Earth. The Sn signature of the Earth's mantle, however, could be affected by core segregation and mantle-crust differentiation processes. Furthermore, global plate tectonics has resulted in extensive recycling of materials between Earth's surface and the mantle for billions of years. Consequently, the mantle records the time-integrated history of recycling lithosphere and its overlying sediments (Hofmann, 1997; Lambart et al., 2019), and is heterogeneous in chemical and isotopic compositions for many elements (Zindler and Hart, 1986).

Metal stable isotopes are increasingly employed to study mantle source heterogeneity and mantle processes (Anguelova et al., 2022; Liu and Li, 2019; Soderman et al., 2022). Significant Sn isotope fractionation has been reported in terrestrial samples (Fig. 1, (Badullovich et al., 2017; Wang et al., 2018)). Tin isotope fractionations have been reported to occur in various processes such as liquid-vapor separation (She et al., 2020; Wang et al., 2019b), redox processes (Polyakov et al., 2005; Roskosz et al., 2020; Wang et al., 2021a), metal–silicate segregation (Kubik et al., 2021), and hydrothermal processes (Liu et al., 2021b; Wang et al., 2019b; Yao et al., 2018). However, there have been no systematic studies on the Sn isotope heterogeneity or homogeneity of the mantle. The previous estimate of Sn isotope compositions of the Earth's mantle was either based on only three OIBs (Ocean Island Basalts) and four Komatiites (Badullovich et al., 2017), or based on only five peridotite and two Mid-ocean ridge basalts (Wang et al., 2018) and these two approaches lead to a difference of about 0.217‰ in $\delta^{122/118}$Sn ratio (Fig. 1). These samples are not sufficient enough for a confident characterization of the Sn composition of the Earth's mantle.

Mid-ocean ridge basalts (MORBs) are the most abundant mafic rocks on Earth and an accessible window into the mantle (Arevalo and McDonough, 2010). They cover the global ocean floor along 60,000 km of ridges (Niu, 2016). The global ridge system samples the mantle and produces two-thirds of the Earth's crust (Gale et al., 2013). Therefore the composition of MORB samples is representative of the oceanic crust, which is the Earth's most extensive crustal reservoir (Arevalo and McDonough, 2010; Gale et al., 2013). MORBs have long been used to investigate the chemical and isotopic heterogeneity of the oceanic upper mantle (Hart, 1988; White, 1985). In this study, we performed high-precision Sn isotope analysis on 27 well-characterized MORBs. These samples are from diverse localities and exhibit considerable chemical variabilities, which provide an opportunity to evaluate how mantle heterogeneity and magmatic processes can affect the Sn isotope compositions of the rocks. After discussing the origin of some Sn isotopic variations, these data are used to provide constraints for the Sn isotope composition of depleted MORB mantle (DMM), where MORBs are sourced from.

2. Samples and analyses

2.1. Background of samples

Well-characterized MORB samples of geographical and compositional diversity were selected for this study. Five different USGS (United States Geological Survey) rock standards are processed along with the MORBs samples for comparison, which are BHVO-2, a basalt from Kilauea, Hawaii, USA; BCR-2, a basalt from Columbia River, Oregon, USA; AGV-2, andesite from Guano Valley, Oregon, USA; GSP-2, a granodiorite from Silver Plume, Colorado, USA; and RGM-2, rhyolite from Glass Mountain, California, USA. The elemental compositions of these reference materials have been reported in detail (Cotta and Enzweiler, 2013; Jochum et al., 2016; Weis et al., 2005).

Based on the relative plate motion rates, mid-ocean ridges are classified into ultrafast, fast, intermediate, slow, and ultraslow spreading ridges (LaFemina, 2015). The spreading rate of the Pacific-Antarctic Ridge (PAR) sections is 94 mm/y (Clog et al., 2013; DeMets et al., 1990; Labidi et al., 2014), while the South West Indian Ridge (SWIR) is an ultraslow spreading ridge with a spreading rate of 14 mm/yr (DeMets et al., 1994; Dick et al., 2003; Sauter et al., 2001). The spreading center of the Central Indian Ridge (CIR) has an intermediate rate of 34–55 mm/yr (DeMets et al., 1990; DeMets et al., 1994; Pak et al., 2017; Van Dover et al., 2001). The spreading rate along the East Pacific Rise (EPR) is about 90 to 150 mm/yr (Brandl et al., 2012; Rea, 1977; Vithana et al., 2019; Zeng et al., 2021). The spreading rate of the Mid-Atlantic Ridge (MAR) segment is 20 to 30 mm/yr (Grindlay et al., 1998). Basalt samples from the ridges mentioned above were selected for this study to cover a wide range of spreading rates.

Most of the MORB samples investigated here are collected from "zero-age" oceanic ridges in different oceans (Fig. 2) and were available at the Institut de Physique du Globe (IPGP) collection. The descriptions of MORBs analyzed in this study can be found in Appendix A of Electronic Supplementary Information (ESI), and the latitude and longitude are listed in Table 1. Except for the DSDP samples from the Atlantic Ocean, the studied samples are fresh glasses (quenched melts), which display large variations in chemical compositions (Table S1, S3) and cover a large range of spreading rates. One Atlantic Ocean sample DSDP-51A-417A-24 underwent extensive alteration. The samples are all basaltic based on the major elemental contents. Some of our samples have been studied for major and trace elements, radiogenic Sr, Nd, Hf isotopes, and stable S, Fe, K, Zr, Ti, Sr, Mo, and Cu isotope compositions (Amsellem et al., 2018; Bezard et al., 2016; Chauvel and Blichert-Toft, 2001; Deng et al., 2018; Hamelin et al., 2011; Inglis et al., 2019; Labidi et al., 2014; Savage et al., 2015; Teng et al., 2013; Tuller-Ross et al., 2019), which were compiled in Table S1 (italic font).

2.2. Major and trace elements measurements

All laboratory work was performed in a class-100 clean room environment at the Institut de Physique du Globe de Paris (IPGP), France. Clean MORB glass fragments were handpicked and powdered with an agate mortar. Pre-cleaned Teflon beakers were used for all samples and solutions processed in this study. Analytical reagent (AR) grade acids were further purified by sub-boiling distillation. Acid and sample solutions were diluted in ultra-pure (18.2 MΩ) Milli-Q water. Elemental measurements were performed for all the MORB samples following a well-established protocol (Deng et al., 2020; Inglis et al., 2019). For each sample, around 50–100 mg of rock powder were digested in 2 ml HF and 4 ml HNO_3 in a capped 30 ml Savillex Teflon beaker that was heated in a box-type hotplate at 130 °C for four days. Then the sample was evaporated at 100 °C to dryness and refluxed with 4 ml 6 N HCl at 130 °C for four days to decompose any remaining fluoride precipitates. The sample was finally dried at 85 °C and re-dissolved in 4 ml 0.5 N HNO_3. All samples were checked to be clear solutions ready for elemental determinations. An aliquot of the solution was diluted by a factor of 5000 and 2000 for major and trace elemental analysis. Concentration measurements for major and trace elements were performed using an Agilent quadrupole inductively coupled plasma mass spectrometer (Q-ICP-MS). Scandium and indium were used for the correction of matrix effects and signal drift during ICP-MS analyses. Certified standards with concentration gradients were prepared to generate calibration curves for concentration calculations. It should be noted that Sn concentrations reported in this study are derived from isotope dilution mass spectrometry associated with the isotopic measurements (see below).

2.3. Sn isotope measurement

Stable Sn isotope analysis was conducted following the method described in Creech et al. (2017) and is summarized here. Roughly 1 g (to obtain between 0.5 and 1 μg Sn) rock powder was weighed and placed in a 30 ml Teflon beaker. Prior to digestion, each sample was mixed with a ^{117}Sn—^{122}Sn double-spike solution to generate an optimal spike-to-sample ratio of approximately 40:60. The mass of spike added to the sample was calculated based on prior Sn concentration data by quadrupole (Q)-ICP-MS. The spiked sample was then digested with a

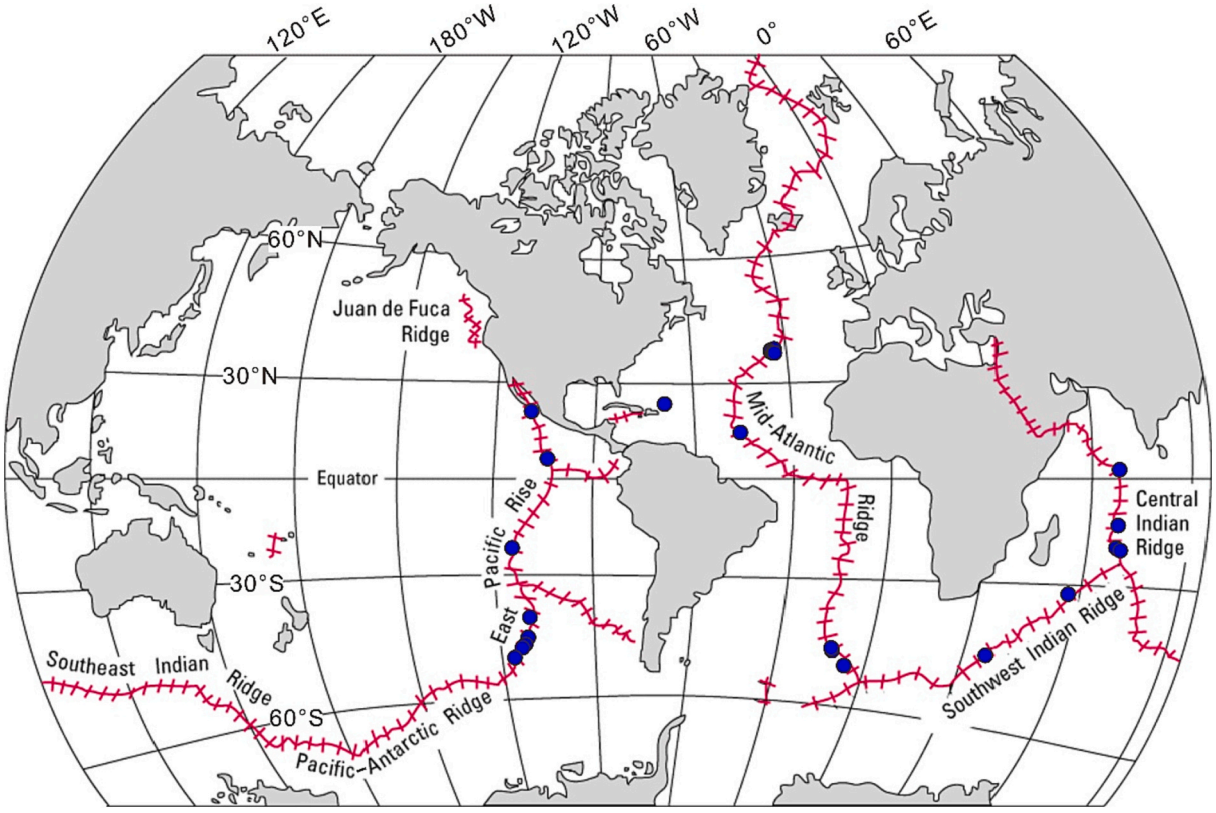

Fig. 2. World map showing the locations of the mid-ocean ridge basalts (MORBs) investigated in this study.

mixture of 1:1 of concentrated HF-HNO_3 on a hotplate at 140 °C for three days. Following initial decomposition, the solution was evaporated to dryness at 60 °C and brought up in concentrated HNO_3, then in 6 N HCl to reflux at 130 °C for two days before drying again at 60 °C. Afterwards, the residues were re-dissolved in 2–4 ml 0.5 N HCl and ready for column chemistry.

Biorad columns filled with 1.5 ml Eichrom TRU resin were used for the purification of Sn. After loading, the matrix elements were eluted with 0.5 N and 0.25 N HCl. Then Sn was recovered using 10 ml 0.5 N HNO_3 as described by Creech et al. (2017). 100 μl of concentrated HF was added to each collection beaker to prevent Sn hydrolysis. The collected Sn solution was dried at 60 °C and taken up in 0.5 N HCl to reach a Sn concentration of 100 ng/g.

Isotope ratio measurement for Sn was performed on a Thermo-Fisher Neptune Plus multiple-collector inductively-coupled-plasma mass-spectrometer (MC-ICP-MS) operated on low-resolution mode. Tin solutions were introduced into ICP using an ESI Apex HF desolvation system using a PFA nebulizer at an uptake rate of 100 μL min^{-1}. Before each isotope analysis, the on-peak zero of acid blanks was measured after rinsing by three tubes of 0.5 N HCl. Optimally spiked standards were bracketed between every two samples. Data reduction was carried out with Isospike (www.isospike.org) tool (Creech et al., 2017; Creech and Paul, 2015) using Iolite software. The raw data were checked to avoid high baseline and interferences. Isotopic results are reported with delta notation as $\delta^{122/118}$Sn relative to the Sn_IPGP standard. The total procedural blank was lower than 1 ng and was insignificant compared to the Sn from the samples. The intermediate precision of the method was ensured by full (dissolution and chemical separation) replicates of GSP-2 and are at the level of 0.069 ‰ (2SD) (Table S2).

3. Results

3.1. Elemental results

Some of the samples analyzed in this study had previously been analyzed for elemental concentrations by Inglis et al. (2019), and both datasets are consistent (See Table S1, S3). The major element results are displayed in Table S1. The major element compositions were adopted from the literature if they existed, and our data were also listed for comparison (Table S1). The major element compositions span around the global MORB means (Gale et al., 2013) and overlap with fresh global MORBs (Fig. 3). Samples vary in chemical compositions, with Mg, Ti, and K abundance ranging from 3.06 to 10.43 wt% MgO, 0.86 to 2.01 wt % TiO_2, and 0.03 to 6.38 wt% K_2O for these samples (Fig. 3). In our sample set, TiO_2 contents increase slightly with decreasing MgO, while the K_2O contents are scattered and do not define a clear array. There is no significant difference in major elements between MORBs from different sites, but the K_2O contents and K_2O/TiO_2 (Fig. S1) ratios appear to be higher in the MAR samples.

The Sn contents of MORB samples range from 0.53 to 2.69 μg/g (Fig. 4), which overlap with those of global MORBs. The Atlantic Ocean basalts have a Sn concentration range of 0.79 to 0.98 μg/g. The Mid-Atlantic Ridge samples show a larger range in Sn concentrations, from 0.53 to 1.97 μg/g, with an average of 1.19 μg/g. Although the La/Sm ratio from the Mid-Atlantic Ridge differs, the Sn content largely overlaps with MORBs from other ridges (Fig. 4). Basalts from the East Pacific Rise have Sn content of 0.87 to 2.69 μg/g, the highest among the investigated samples. The Sn concentrations are 1.17–1.80 μg/g for Pacific-Antarctic Ridge on-axis basalts and 0.62–1.24 μg/g for off-axis samples. Finally, the Sn concentrations of South West Indian Ridge and Central Indian Ridge on-axis samples are 1.91–2.54 μg/g and 0.69–1.43 μg/g, respectively. In comparison, the Sn content of one off-axis Central Indian Ridge sample is 2.34 μg/g. PM-normalized spider diagrams according to their incompatibility of MORBs from different locations are shown in Fig. 5.

Table 1
Tin isotopic compositions of mid-ocean ridge basalts.

Sample	Location	Age	Location	Latitude	Longitude	$\delta^{122/118}Sn_{IPGP}$	$\delta^{122/118}Sn_{BHVO-2}$	$\delta^{122/118}Sn_{3161a}$	2SD	N	Sn content/ $\mu g \cdot g^{-1}$	$(La/Sm)_N$	spreading rate/ $mm \cdot y^{-1}$
CYP74 31–35	Mid-Atlantic Ridge	0	on-axis	36.85	−33.25	0.198	0.017	0.348	0.031	2	0.53	1.49	25
ARP 74 9 13C COLUMN	Mid-Atlantic Ridge	0	on-axis	36.83	−33.27	0.234	0.053	0.384	0.017	2	1.18	1.27	
ARP 74 78C COLUMN	Mid-Atlantic Ridge	0	on-axis	36.83	−33.25	0.239	0.058	0.389	0.013	2	1.20	1.57	
ARP 74 7 8 SURFACE	Mid-Atlantic Ridge	0	on-axis	36.83	−33.25	0.181	0.000	0.331	0.006	2	1.16	1.57	
CH31-DR12–137	Mid-Atlantic Ridge	0	on-axis	36.84	−33.25	0.217	0.036	0.367	0.033	2	0.90	1.30	
CH30 DR 17–03	Mid Atlantic Ridge	0	on-axis	37.92	−31.10	0.201	0.020	0.351	0.042	4	1.45	2.01	
EW9309 20D-1 g	Mid-Atlantic Ridge	0	on-axis	−51.43	−5.78	0.194	0.013	0.344	0.004	2	1.74	1.47	
EW9309 3D-1 g	Mid-Atlantic Ridge	0	on-axis	−47.795	−10.15	0.235	0.054	0.385	0.012	2	1.17	1.82	
2πD 44–1	Mid-Atlantic Ridge	0	on-axis	~14.3	~ − 45	0.188	0.007	0.338	0.016	2	1.06	1.96	
DSDP-52-417D-55-2	Atlantic Ocean	Cretaceous	on-axis	25.112	−68.047	0.241	0.060	0.391	0.027	2	0.79	0.45	
DSDP-51A-417A-24 (excluded)	Atlantic Ocean	Cretaceous	on-axis	25.1105	−68.0413	0.390	0.209	0.540	0.016	2	0.98	0.61	
DSDP-52-417D-65-6	Atlantic Ocean	Cretaceous	on-axis	25.112	−68.047	0.253	0.072	0.403	0.004	2	0.92	0.47	
SWIFT DR06–3-6 g	South West Indian Ridge	0	on-axis	−44.90	36.47	0.193	0.012	0.343	0.010	2	1.91	1.48	14
MD34 D1	South West Indian Ridge	0	on-axis	−31.69	57.84	0.300	0.119	0.450	0.076	2	2.54	0.91	
MD57-D6–7	Central Indian Ridge	0	on-axis	−15.89	67.28	0.190	0.009	0.340	0.042	2	0.85	0.79	48
MD57 D13	Central Indian Ridge	0	on-axis	1.47	67.64	0.218	0.037	0.368	0.066	2	1.43	0.72	
MD57 D3–3	Central Indian Ridge	0	on-axis	−20.16	66.84	0.245	0.064	0.395	0.004	2	0.69	0.61	
MD57 D2–8	Central Indian Ridge	0	off-axis	−21.72	69.29	0.310	0.129	0.460	0.018	2	2.34	0.58	
CYP78 12–34	East Pacific Rise	0	on-axis	20.90	−109.05	0.206	0.025	0.356	0.025	2	0.87	0.67	145
SEARISE1 DR04	East Pacific Rise	0	on-axis	6.73	−102.60	0.265	0.084	0.415	0.008	2	2.69	0.62	
SEARISE2 DR03	East Pacific Rise	0	on-axis	−21.41	−114.28	0.291	0.110	0.441	0.008	2	1.29	0.48	
PAC2 DR43-5G	Pacific-Antarctic Ridge	0	off-axis	−40.54	111.03	0.230	0.049	0.380	0.040	2	0.62	0.48	94
PAC2 DR32-1 g	Pacific-Antarctic Ridge	0	on-axis	−45.39	112.43	0.130	−0.051	0.280	0.015	2	1.80	0.72	
PAC2 DR28-2G		0	on-axis	−47.51	113.25	0.174	−0.007	0.324	0.096	2	1.17	0.55	

(*continued on next page*)

Table 1 (*continued*)

Sample	Location	Age	Location	Latitude	Longitude	$\delta^{122/118}Sn_{IPGP}$	$\delta^{122/118}Sn_{BHVO-2}$	$\delta^{122/118}Sn_{3161a}$	2SD	N	Sn content/ $\mu g \cdot g^{-1}$	$(La/Sm)_N$	spreading rate/ $mm \cdot y^{-1}$
PAC2 DR25-1G	Pacific-Antarctic Ridge	0	off-axis	−48.61	114.79	0.268	0.087	0.418	0.014	2	1.17	0.76	
PAC2 DR16–7G	Pacific-Antarctic Ridge	0	off-axis	−50.20	115.89	0.263	0.082	0.413	0.068	2	1.06	0.74	
PAC2 DR16–1G (excluded)	Pacific-Antarctic Ridge	0	off-axis	−50.20	115.89	0.283	0.102	0.433	0.076	2	1.24	0.73	

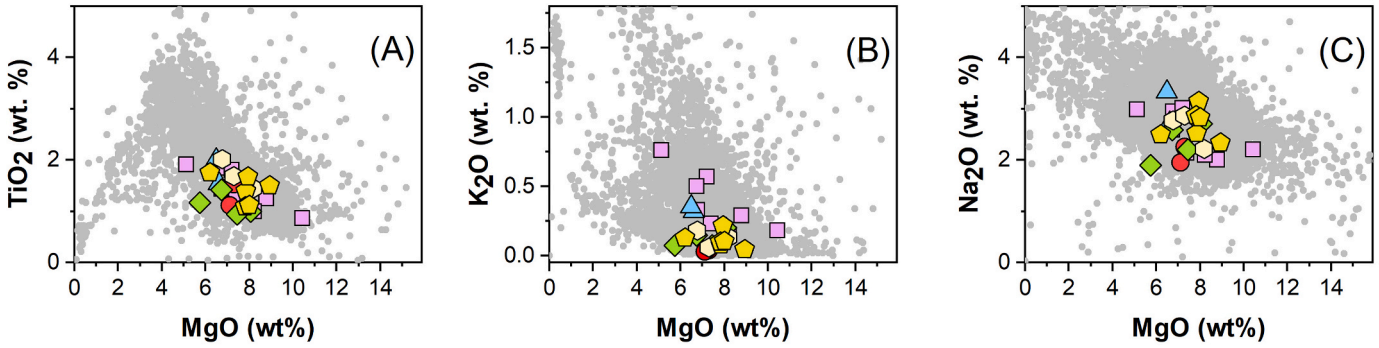

Fig. 3. MORB samples analyzed in this study are plotted over the global MORB dataset (gray) for (A) TiO_2 vs. MgO, (B) K_2O vs. MgO, and (C) Na_2O vs. MgO. Major element data for samples are from PetDB and this study. All the data follow the first-order liquid line of descent (LLD) trends defined by global MORBs during MORB melt cooling and evolution. The global MORB dataset was downloaded from PetDB on 15 December 2021 (https://search.earthchem.org/) using parameters: "spreading center; basalt; fresh." The legends are the same as in Fig. 3.

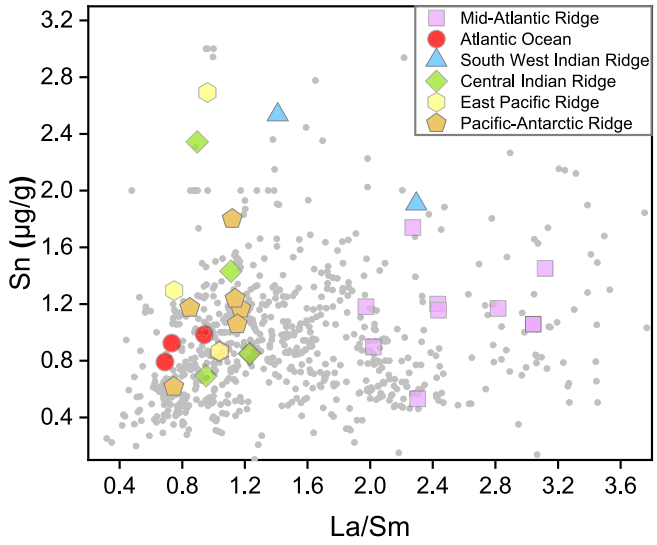

Fig. 4. The relationship between Sn concentration and La/Sm ratio (unnormalized) of MORB samples. The data were downloaded from the PetDB Database (www.earthchem.org/petdb) on 13 September 2022, using the following parameters: "spreading center; basalt; fresh."

All samples analyzed in this study display similar patterns with *E*-MORBs and N-MORBs from Sun and McDonough (1989). The composition variability of the studied MORB samples is more profound for incompatible elements (Fig. 5).

3.2. Tin isotopic results of Sn standards and MORBs

There are different reference materials for the expression of Sn isotopic results with different batch numbers in the literature (Fig. 1). Due to the lack of certified international Sn isotopic reference materials, the IPGP group first used an ICP PLASMAL solution as a reference standard, labeled as "Sn_IPGP." At the same time, the single elemental standard NIST 3161a was also used by researchers. The repeated measurements of IPGP standards against itself return a $\delta^{122/118}Sn_{IPGP}$ value of 0.000 ± 0.030‰ ($N = 129$). We also doped the IPGP standard with the matrix of granites and basalts and treated them as unknown samples to validate the accuracy of the method. The IPGP standard doped with major elements similar to typical basalt and granite and then processed through chemistry returned a $\delta^{122/118}Sn_{IPGP}$ value of −0.017 ± 0.014‰ ($N = 2$) and − 0.014 ± 0.004‰ (N = 2), respectively. The NIST 3161a from Nanjing University has a $\delta^{122/118}Sn_{IPGP}$ of −0.150 ± 0.059‰ ($N = 11$). After the NIST 3161a is passed through the whole chemical purification procedure, it returns the $\delta^{122/118}Sn_{IPGP}$ values of −0.171 ± 0.003‰ (N = 2) and − 0.175 ± 0.011‰ ($N = 3$) with and without the addition of HF acid in the pure solution before loading on the column chemistry, which are all identical within error and also consistent with the value reported in She et al. (2020) (−0.17 ± 0.06‰, Lot #140917). However, it should be noted that the lack of a common isotopic standard and the difference in some of the isotopic notations has hampered confident inter-laboratory comparison. Except for BHVO-2 and BCR-2, other common rock standards were measured only once by Creech et al. (2017). More recently, Wang et al. (2022) reported a large discrepancy between Sn isotope data for geostandards such as BHVO-2 measured by different labs, which was explained by insufficient replication, heterogeneity of the BHVO-2, or different Lots of Sn_IPGP. Similar heterogeneity of geostandard GPt-3 was reported for Mo isotopes (Fan et al., 2020).

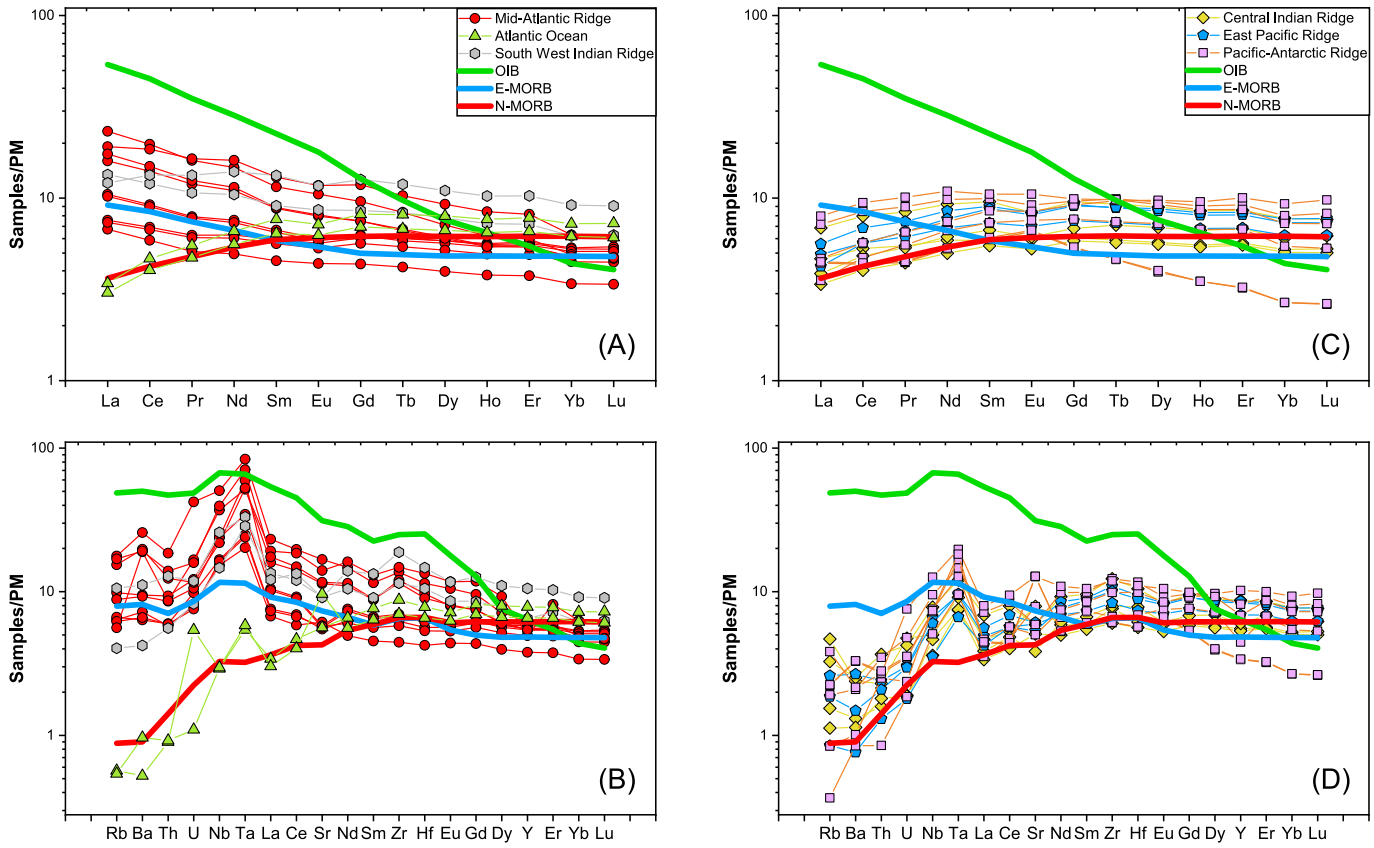

Fig. 5. PM-normalized incompatible element concentrations of MORBs analyzed in this study, along with OIB, *E*-MORB, and N-MORB composition from Sun and McDonough (1989). The order of trace-element incompatibility and PM composition are from Sun and McDonough (1989). PM = primitive mantle.

To better characterize the geostandards, several separate repeated dissolutions of BHVO-2, BCR-2, GSP-2, and multiple measurements of each rock standard were carried out (Table S2). The typical overall yield of Sn for the samples was around 50%. The actual sample-spike ratios varied from 35%–45%. Over the course of this study, analyses of these rock standards yielded $\delta^{122/118}Sn_{IPGP}$ values of 0.181 ± 0.066‰ for BHVO-2 ($N = 12$; 0.331 ± 0.066‰ in $\delta^{122/118}Sn_{3161a}$), 0.134 ± 0.038‰ for BCR-2 ($N = 16$; 0.284 ± 0.038‰ in $\delta^{122/118}Sn_{3161a}$), 0.074 ± 0.069‰ for GSP-2 (N = 12; 0.224 ± 0.069‰ in $\delta^{122/118}Sn_{3161a}$), 0.147 ± 0.006‰ for AGV-2 ($N = 9$; 0.297 ± 0.006‰ in $\delta^{122/118}Sn_{3161a}$), and 0.002 ± 0.051‰ for RGM-2 ($N = 2$; 0.152 ± 0.051‰). There is a systematic negative shift by around 0.2‰ for these rock standard values compared to the data reported by Creech et al. (2017). Since we used a similar procedure as in Creech et al. (2017), including the same double spike solution, one possible explanation for this discrepancy could be the sample heterogeneity of the rock powders (Weis et al., 2005), as we used different jars of the geostandard powders. Another possible issue is that the original concentrated Sn_IPGP standard stock solution was depleted before this study, and we used an old diluted (1 μg/g) solution remaining in a previously-used bottle to prepare the 100 ng/g in-house bracketing standard solution for MC-ICP-MS analyses. Since aqueous Sn is susceptible to hydrolysis, it is possible that the isotopic composition of the 1 μg/g old and dilute IPGP standard solution had been affected by partial hydrolysis during storage. The difference in reported Sn isotope data between different laboratories or researchers could also be related to experimental procedures. The Sn isotope compositions of natural samples could be altered during sample dissolution (Berger et al., 2018), if volatilization of Sn (Mathur et al., 2017; She et al., 2020; Wang et al., 2019b) occurs before sample-spike equilibration.

It is important to note that when we convert all the data relative to BHVO-2, the meteorite CV3 and L4 of Wang et al. (2021b) are consistent with Creech and Moynier (2019) within error (Table S2). This implies systematic, but consistent and correctable, offsets in measured $\delta^{122/118}Sn$ for geostandards between different laboratories. It should be noted that our results relative to NIST 3161a is consistent with Wang et al. (2022) and She et al. (2023), which validate the quality of our data (Table S2). Therefore, both NIST 3161a and BHVO-2 from different laboratories are expected to be homogeneous in Sn isotope compositions. Thus, to avoid potential problems with the conservation of standards, we report all the data relative to the measured average value of the BHVO-2 ($n = 12$) and NIST 3161a simultaneously and renormalize all the literature data relative to the corresponding literature BHVO-2 and NIST 3161a to allow inter-laboratory comparison. We suggest that until a certified Sn isotopic standard is recognized among community, each study analyzes the Sn isotopic composition of both BHVO-2 and NIST 3161a and uses them as anchoring points. Therefore, all the data will be discussed here as $\delta^{122/118}Sn_{BHVO-2}$ and $\delta^{122/118}Sn_{3161a}$.

The Sn isotope data for MORB samples are tabulated in Table 1, Fig. 6A and Fig. 7. The MORB samples display an analytically resolvable range of $\delta^{122/118}Sn_{BHVO-2}$ from −0.051 ± 0.015‰ to 0.209 ± 0.016‰ ($\delta^{122/118}Sn_{3161a}$ of 0.280 ± 0.015‰ to 0.540 ± 0.016‰), with an average $\delta^{122/118}Sn_{BHVO-2}$ of 0.054 ± 0.105‰ ($\delta^{122/118}Sn_{3161a}$ of 0.385 ± 0.105‰) (2SD, $n = 27$).

4. Discussion

4.1. Tin isotope behaviors during secondary alteration

The pristine MORB samples can be used to study the Sn isotopic composition of upper mantle-derived melts. However, the basalts are prone to contamination by alteration involving dissolution, diffusion, and adsorption processes (Jenner and O'Neill, 2012), which could overprint the primary signatures of the original basalt. The alteration of oceanic crust leads to relatively limited Cu, Zn, and V isotope

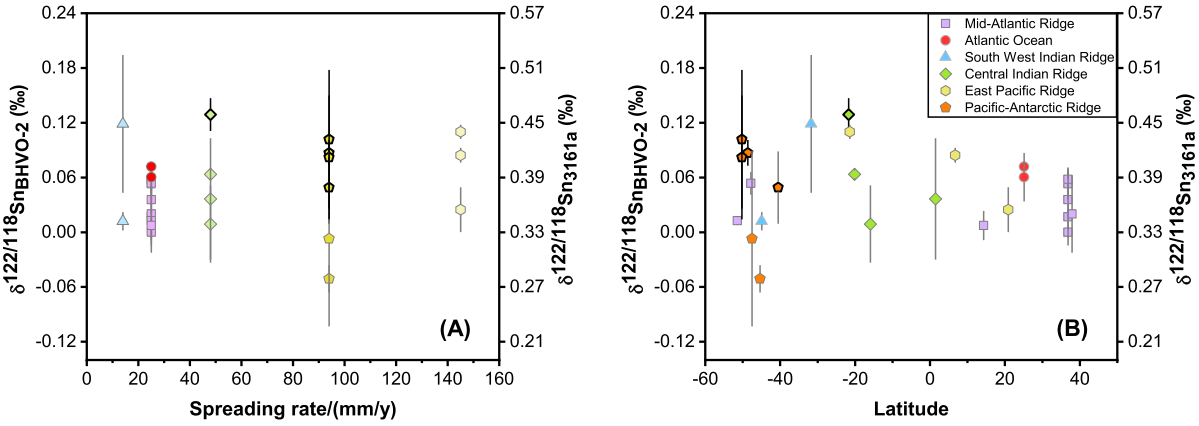

Fig. 6. The Sn isotope compositions against mid-ocean ridge spreading rates (a); latitudes (b) for MORBs investigated in this study. The off-axis samples are represented by thicker black edges.

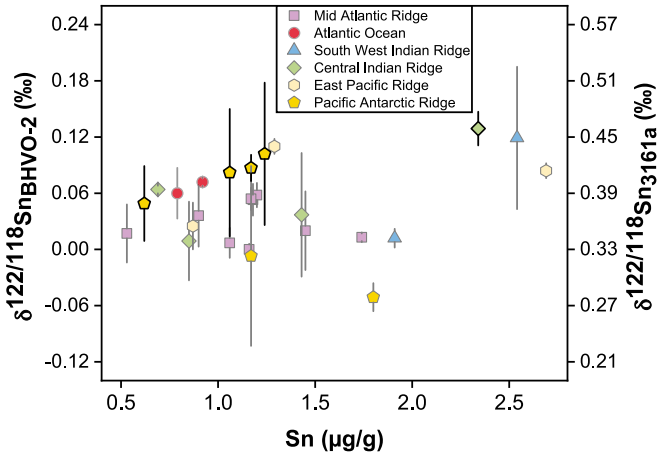

Fig. 7. The plot of Sn isotope compositions versus Sn contents for MORBs analyzed in this study.

fractionations (Huang et al., 2016; Wu et al., 2018) but significantly fractionate K, Fe, and Zn isotopes (Liu et al., 2021a; Rouxel et al., 2003; Tuller-Ross et al., 2019).

In contrast to the fresh basalts from DSDP Hole 417D, Hole 417A was highly altered by seawater circulation (Byerly and Sinton, 1980; Emmermann and Puchelt, 1980). The chemical index of alteration (CIA) and loss on ignition (LOI) can be used to reflect the degree of alteration (Bienvenu et al., 1990; Liu et al., 2021a). The sample DSDP-51A-417A-24 is significantly altered with a high CIA (0.59) value (Fig. S2) and high LOI (4.75%) value, as well as an enrichment in K_2O (6.38 wt%). DSDP-51A-417A-24 is remarkably enriched in heavy Sn isotopes with a $\delta^{122/118}Sn_{BHVO-2}$ value of 0.209 ± 0.016‰ ($\delta^{122/118}Sn_{3161a}$ of 0.540 ± 0.016‰), the heaviest values measured in this study. The major elements of the two samples from 417D plot within the fields of fresh global MORBs (Fig. 3), and the CIA values are similar to other fresh basalts (Fig. S2). The Sn isotope compositions of two samples from hole 417D are ($\delta^{122/118}Sn_{BHVO-2}$ from 0.074 ± 0.027‰ to 0.086 ± 0.004‰ ($\delta^{122/118}Sn_{3161a}$ of 0.405 ± 0.027‰ to 0.417 ± 0.004‰)) close to that of modern MAR samples and the average MORBs.

Hydrothermal circulation of seawater through the oceanic crust is common (German and Seyfried, 2014; Staudigel, 2014). The altered basalts could be potential sources and sinks of Sn for seawater (Schmidt et al., 2011), as the more altered margins of basalts could be either enriched or depleted relative to the less-altered cores in Sn concentrations (Jochum and Verma, 1996). Because Sn concentrations in seawater range from pg/g to ng/g level (Abdel Ghani, 2015; Byrd and Andreae, 1982; Sun and Li, 2015), Sn from fresh seawater during basalt-seawater interaction is unlikely to be a dominant contributor to the Sn budget in the altered basalts. The enrichment of Sn in altered basalts was proposed to originate from the modified seawater by overlying Sn-rich sediments (Jochum and Verma, 1996). It is more likely that the lighter Sn isotopes were preferentially stripped out of the basalts at Hole 417A by the heated seawater. Sulfides are thought to hold isotopically lighter Sn (Badullovich et al., 2017; Yao et al., 2018). The loss of isotopically light Sn through sulfide dissolution in basalt might also be an explanation, although this cannot be tested in the present study, and more systematic analyses of altered basalt samples and maybe detailed basalt leaching experiments are needed. Nonetheless, because alteration caused secondary Sn isotope variation, the altered basalt sample is excluded in the following discussions (DSDP- 51A-417A-24 from the Atlantic Ocean in Table 1; Fig. S2, the point with the largest size).

4.2. Behavior of Sn isotopes during magma differentiation and partial melting

The Mid-Atlantic ridge-derived MORBs are enriched in incompatible elements and light Rare-Earth elements (LREE) (Fig. 5A, B), while Pacific MORBs are relatively depleted in LREE and elements such as Th, Ba (Fig. 5C, D). The MORB samples from this study have a wide range of MgO contents (5.12–10.43 wt%), and they follow liquid lines of descent (LLD) of global MORBs (Klein and Langmuir, 1987; Niu, 2016; White and Klein, 2014), as shown in Fig. 3A (also seen in CaO and TiO_2 contents compiled in Table S1). During MORB evolution, Sn could reside in minerals like olivine, clinopyroxene, plagioclase, and spinel (Adam and Green, 2006; Badullovich et al., 2017; Michely et al., 2017; Sato, 2004). The lack of correlation between Sn concentrations and La/Sm (Fig. 4) suggests that the Sn contents of MORBs are not influenced by partial melting processes (Kamenetsky and Eggins, 2012). Instead, the increase in Sn concentrations with decreasing MgO contents (Fig. 8A) implies the incompatible behavior of Sn during MORB melt evolution, and the dominant control of fractional crystallization on the bulk-rock Sn concentrations.

The $\delta^{122/118}Sn$ values do not systematically vary with MgO content for all samples (Fig. 8B). Badullovich et al. (2017) proposed crystallization of Fe—Ti oxides below ~5 wt% MgO could lead to resolvable Sn isotope fractionation. The absence of Sn isotope fractionation associated with MgO variations in this study may be because Fe—Ti oxides did not reach the onset point of crystallization for the MORB samples investigated here (Coogan, 2014; Deng et al., 2019; Deng et al., 2018) since the MgO contents of our samples were higher than 5 wt%. Fractional crystallization of Fe—Ti oxides is suggested to begin after MgO is dropped to

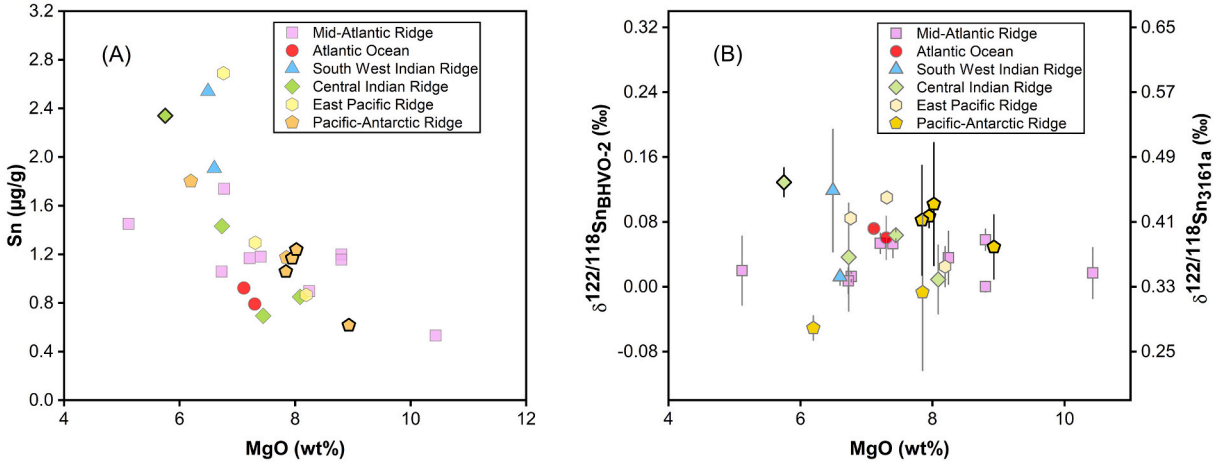

Fig. 8. (A) Variations of Sn contents among different MgO concentrations, (B) the relationship of Sn isotope compositions and MgO (wt%) among all fresh MORB samples. These figures demonstrate the effect of mineral fractionation on Sn elemental and isotopic behaviors. The off-axis samples are marked by thicker black edges.

3 wt% in MORB systems (Chen et al., 2019b). The lack of correlation of Sn isotope value with Sn contents (Fig. 7), which had been reported by Wang et al. (2018), can be explained by the source heterogeneity, melt depletion, and/or mixing process.

Sulfur is heterogeneously distributed in the upper mantle, where sulfide saturation is common during MORB generation, and sulfides can stay in a molten state for the MORB mantle melting conditions (Sun et al., 2020; Wang et al., 2018; Zhang and Hirschmann, 2016). Most sulfides could enter the melt during a high degree of partial melting (Peach et al., 1990; Sun et al., 2020), and Sn could be enriched in sulfides with high distribution coefficients (Badullovich et al., 2017; Greaney et al., 2017; Jenner, 2017; Li and Audétat, 2012; Patten et al., 2013; Wang et al., 2018; Yi et al., 1995), but the isotopic fractionation behavior between silicate and sulfides have not been documented. For the SWIR, EPR, and PAR samples analyzed in this study, there is no correlation between Sn isotope composition and Cu content (Fig. 9A). However, basalt samples of CIR exhibit a significant correlation between $\delta^{122/118}$Sn value and Cu concentration (Fig. 9B; $R^2 = 0.9919$, linear regression analysis $p = 0.0149 < 0.05$), and a similar correlation can be observed for chalcophile element Co as well. There is also a plausible weak correlation between $\delta^{122/118}$Sn value and Cu concentration for MAR samples, given one sample (EW9309 20D-1 g) with the highest Cu content is excluded. Data from CIR and MAR basalts imply that the sulfide-enriched samples could have lighter Sn isotope composition compared to those depleted in sulfides. This could be attributed to the long bond length of Sn—S in sulfides, which would enrich lighter Sn isotopes for Cu-bearing sulfides (Badullovich et al., 2017; Wang et al., 2018; Yao et al., 2018). Segregation of sulfide can occur due to a decrease of pressure during ascent and evolution prior to eruption, driving the magma toward sulfur under-saturation (Patten et al., 2013). The coexistence of sulfides and basalt glass has been reported for MORBs (Patten et al., 2013; Peach et al., 1990). Therefore, it is likely the samples of low contents experienced the segregation of sulfide and removal of lighter Sn isotopes. We acknowledge that such observation and interpretation are preliminary and require more future work for confirmation.

Seafloor spreading is a fundamental process for plate tectonics that links mantle convection and the production of the oceanic crust and mantle lithosphere (Buck and Poliakov, 1998; Elsasser, 1971; Estep et al., 2021). The spreading rate could affect magmatic processes. For example, more melt will be supplied to shallow magma chambers, where more extensive fractional crystallization occurs at fast-spreading ridges, producing more differentiated magmas (Chen et al., 2020; Michael and Cornell, 1998; White and Klein, 2014). A higher spreading rate could lead to a larger extent of mantle melting and thus attenuate potential mantle heterogeneities (Chauvel and Blichert-Toft, 2001; Niu, 2016; Niu and Hékinian, 1997b). Basalts from mid-ocean ridge segments of different spreading rates provide an opportunity to test the impact of the spreading rate on Sn isotope fractionation. As shown in Fig. 6, there is no trend between basalt Sn isotope composition and the spreading rate, and

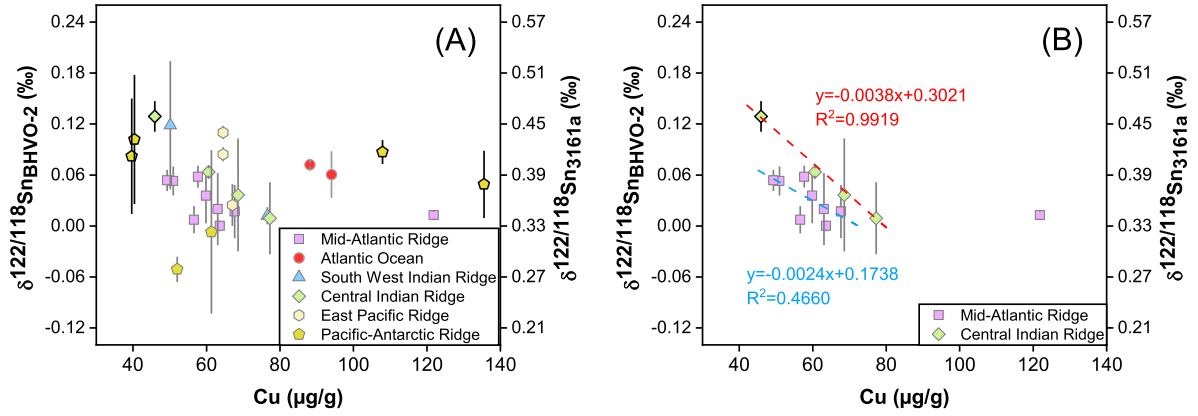

Fig. 9. (A) Plot of Sn isotope compositions versus Cu (μg/g) contents of the MORBs analyzed in this study. (B) The relationship of Sn isotopic values as a function of Cu contents for MORBs from MAR and CIR.

the latitude of the segment.

In order to evaluate the potential effect of partial melting on Sn isotopes in MORBs, we calculated $Na_{8.0}$ for the samples, an index of partial melting (Klein and Langmuir, 1987), known to increase with axial depth arising from temperature difference or compositional variation of deep ridges to shallow ridges (Niu and O'Hara, 2008; White and Klein, 2014). $Na_{8.0}$ represents the Na_2O content corrected to a MgO content of 8 wt% (for MgO content from 5 to 8.5 wt%, which is the case for most samples in this study). Since our samples are fresh glasses, the effect of volatiles on the calculation of $Na_{8.0}$ can be neglected. Variation in $Na_{8.0}$ values should, theoretically, only result from partial melting (Saunders et al., 2022), with a higher value corresponding to a lower extent of melting (Coogan, 2014). For the basalt samples in this study, there is no significant correlation between $\delta^{122/118}Sn$ and $Na_{8.0}$ values (Fig. 10), which indicates that partial melting is not responsible for Sn isotope fractionations during MORB generation and evolution. This agrees with Wang et al. (2018), who observed that no clear relationship between Sn isotope composition and the degree of melting for mantle-derived basalts.

The K_2O/TiO_2 ratios could be used as a proxy for the degree of source enrichment (Marty and Zimmermann, 1999; Teng et al., 2013; Tomascak et al., 2008; Tuller-Ross et al., 2019), and higher K_2O/TiO_2 ratios correspond to higher La/Sm ratios (Fig. S1). The lack of correlation between $\delta^{122/118}Sn$ values and the K_2O/TiO_2 ratios demonstrates that the source enrichment may not affect the Sn isotopic composition of MORBs.

The on-axis magmas are sourced from a partially molten mantle beneath the ridge axis (Stracke, 2021), whereas off-axis magmas are formed several km away from the axis (for example, the PAR off-axis seamounts could be 10 to 300 km away from the ridge) and have a non-hotspot origin triggered by kinematic change and decompression melting of the mantle (Labidi et al., 2014). At on-axis ridges, the large volume of mantle melting and magma mixing can homogenize the erupted magma compositions (Brandl et al., 2012). In contrast, the off-axis seamount samples are likely to record greater chemical variability (Brandl et al., 2012), sampling upper mantle heterogeneity preserved from melting smaller volumes of the mantle. The off-axis sample PAC2 DR 16-1 g, which had the higher $^{87}Sr/^{86}Sr$ and lower $^{143}Nd/^{144}Nd$ isotopes (Fig. S3, Table S1), was associated with the highest Mo (Bezard et al., 2016) and high $\delta^{122/118}Sn$ values. The effect of degassing and contributions from HIMU of off-axis samples (Bezard et al., 2016; Leroux et al., 2006; Sano and Yamashita, 2019) could account for the isotopic difference and are worthy of further investigation, but these effects are beyond the scope of this study. Because of that, the off-axis sample PAC2 DR 16-1 g from PAR was excluded in the following statistical analysis.

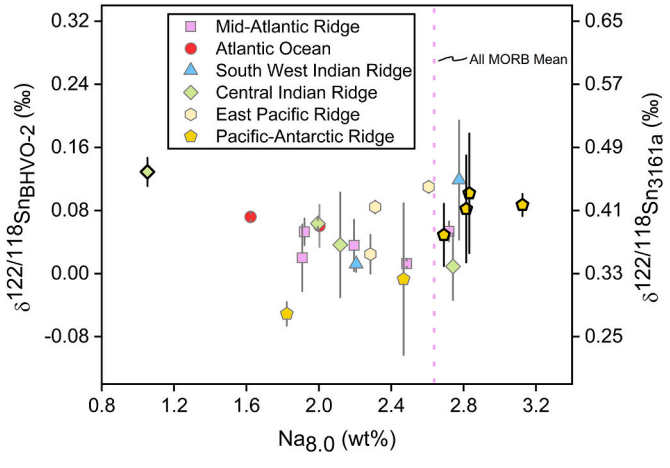

Fig. 10. Sn isotope compositions versus $Na_{8.0}$. $Na_{8.0}$ are calculated for samples with MgO between 5 and 8.5 wt% only, using the equation $Na_{8.0} = Na_2O + 0.373 * (MgO) - 2.98$. The off-axis samples are represented by thicker black edges. All MORB mean $Na_{8.0}$ deduced from data of Gale et al. (2013) is marked as vertical dash line, with global MORB regional average $Na_{8.0}$ ranging from 1.67 to 3.58 (Klein and Langmuir, 1987; White and Klein, 2014).

4.3. Statistical tests for the Sn isotopic heterogeneity of MORB

In the following discussion, MORBs are separated into two groups based on normalized La/Sm ratios with reference to chondrite compositions proposed by Sun and McDonough (1989) (Fig. 11). Normal-MORB (N-MORBs) samples are defined as $(La/Sm)_N$ lower than 1, whereas enriched-MORBs (E-MORBs) are characterized by maximum $(La/Sm)_N$ higher than 1 (Saccani et al., 2022; Saunders et al., 2022). Most of the E-MORBs of this study are from the Mid-Atlantic Ridge and are characterized by higher K_2O content, which is consistent with the higher global mean K_2O contents of E-MORBs compared to N-MORBs (Gale et al., 2013). The origin of enriched MORBs is debated and has been attributed to the addition of melt from the subducted crust or recycled sediment to the source (Nielsen et al., 2018; Yang et al., 2020), the interaction of enriched plumes with normal mid-ocean ridge basalts (Humphris et al., 1985; Ma et al., 2022; Schilling, 1973), low-degree melt metasomatism (Chen et al., 2022; Donnelly et al., 2004; Guo et al., 2023; Waters et al., 2011). The depleted MORBs are the products of melting the depleted mantle (Sun and McDonough, 1989).

The recycled oceanic crust should have low Mo/Ce since Mo is mobilized by fluids during subduction (Chen et al., 2019a; Chen et al., 2022). Recycled sediments or continental crustal materials are enriched in LILE but depleted in Nb relative to elements of similar compatibility (Chen et al., 2022). The similar Th/U and Mo/Ce ratios (Fig. S4A) for E-MORBs and N-MORBs, as well as the simultaneous enrichment of Nb/La and Th in this study (Fig. S4B), preclude the dominant role of recycling in the formation of E-MORBs in this study. Contributions of recycled material from plume to MAR (13.2°S-24.2°S) have been reported (Zhang et al., 2021). Nevertheless, some E-MORBs are irrelevant to hot spot plumes (Borghini et al., 2021; Donnelly et al., 2004; Kim et al., 2017; Ulrich et al., 2012), which makes plume-ridge interaction suitable for only a part of E-MORBs. The lack of correlations between Sn/Ce, Sn/Yb, La/Yb, and $\delta^{122/118}Sn$ values indicates that elemental incompatibility exerts no control on our samples. The *E*-MORBs have tightly distributed $\delta^{122/118}Sn_{BHVO-2}$ value of 0.027 ± 0.043‰ ($\delta^{122/118}Sn_{3161a}$ of 0.358 ± 0.043‰) ($N = 10$). At the present stage, with the current analytical precision and size of data set, Sn isotopes cannot be used to resolve the origin of global E-MORBs.

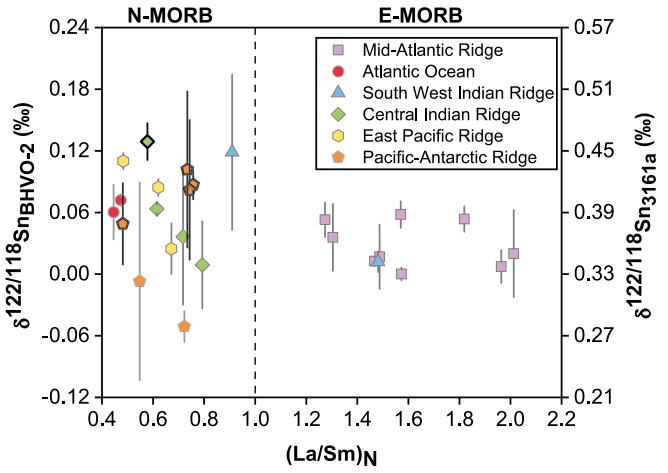

Fig. 11. The Sn isotope data for MORB samples plotted against the primitive mantle normalized La/Sm ratios. The vertical dashed lines represent the boundaries between E-MORBs and N-MORBs. The two standard deviation error is shown for individual measurement. The off-axis samples are represented by thicker black edges.

The Sn isotope compositions of N-MORBs are slightly more scattered compared to E-MORBs. The N-MORBs have $\delta^{122/118}Sn_{BHVO\text{-}2}$ of −0.051 ± 0.015‰ to 0.129 ± 0.018‰ ($\delta^{122/118}Sn_{3161a}$ of 0.280 ± 0.015‰ to 0.460 ± 0.018‰), with an average $\delta^{122/118}Sn_{BHVO\text{-}2}$ value of 0.058 ± 0.098‰ ($\delta^{122/118}Sn_{3161a}$ of 0.389 ± 0.098‰) ($N = 15$). The mantle is subjected to metasomatic effects (Hu et al., 2016; Kang et al., 2017; Poitrasson et al., 2013; Zhao et al., 2015) arising from liquid percolation and subsequent reaction. Magmatic refertilization by reactive melt percolation and melt-peridotite interactions is a widespread phenomenon in a compositionally heterogeneous lithospheric mantle (Chen et al., 2014; Le Roux et al., 2007; Niu and Hékinian, 1997a; Zhang et al., 2009), and could affect the source of MORB (Marchesi et al., 2013). Wang et al. (2018) suggested that peridotite refertilization could increase Sn concentrations and slightly modify the Sn isotope composition. The scattering of N-MORBs data could also be related to the diversity of sampling sites.

Based on the discussions above, MORB generation and evolution processes, except for sulfide segregation, are not likely to markedly fractionate Sn isotopes. Therefore the Sn isotope composition of MORBs could be used to infer the MORB mantle source. Despite the wide geographic dispersion and chemical diversity, all MORBs have similar average Sn isotope compositions. To test the Sn isotopic homogeneity of the MORB source, we carried out an independent *t*-test of Sn isotope compositions. The samples that likely had experienced sulfide segregation from CIR (MD57 D13, D3–3, D2–8) were excluded. A violin plot is used to demonstrate the distribution of Sn isotope composition, with the width and length representing the approximate frequency and the range of Sn isotope composition. As shown in Fig. 12, the E-MORBs and N-MORBs overlap in Sn isotope composition. The normal distribution test is >0.1, satisfying the requirement for the data to perform a t-test. The t-test shows no significant difference between E-MORBs and N-MORBs ($t = -1.5262$, $p = 0.1232$, higher than the threshold of 0.05, and accepts the null hypothesis). Meanwhile, the t-test of the Sn concentration of these groups also shows no difference ($t = -0.3455$, $p = 0.7333$). This likely reflects an efficient mixing or inheritance of a non-evolved average composition of the source, consistent with the homogeneous distribution of Sn content concluded from a previous study (Jochum et al., 1993).

4.4. The Sn isotope composition of MORB mantle source and oceanic crust

The application of Sn isotopes to planetary studies requires an accurate characterization of the composition of the mantle. Measurements of oceanic island basalts (OIBs) could be necessary since they sample a more fertile deeper mantle composition and melts of a smaller degree of partial melting (Bezard et al., 2016). However, it should be noted that the stable isotopic compositions of OIBs are susceptible to the imprint of recycling sediments or altered oceanic crust (Moynier et al., 2021; Pringle et al., 2016), which may complicate the interpretation. In a previous study, the mantle was inferred to have $\delta^{122/118}Sn_{BHVO\text{-}2}$ of 0.042 ± 0.113‰ based on measurements of komatiites and Kilauea Iki (KI) lava lake OIBs (Badullovich et al., 2017). By contrast, Wang et al. (2018) derived a different mantle $\delta^{122/118}Sn_{BHVO\text{-}2}$ value of −0.175 ± 0.055‰ (2SD) based on five peridotites. The difference between previous studies could be due to the fact that OIBs and peridotites sampled greater heterogeneities (Saunders et al., 2022).

Since Sn is a moderately incompatible element, the Sn isotope composition of MORB could sample the depleted mantle rather than the bulk silicate Earth. The sample with the highest degree of melting (i.e., with the lowest $Na_{8.0}$ in Fig. 10) would have Sn isotope composition the closest to the depleted mantle. Specifically, the EPR and PAR (except for PAC 2 DR16-1 g, Fig. S3) samples are characterized by low $(La/Sm)_N$ and $^{87}Sr/^{86}Sr$ ratios, high $^{143}Nd/^{144}Nd$ ratios (PetDB database) (Table S1, Fig. S3), potentially representing a part of depleted MORB mantle (DMM) source. Therefore, the fresh MORBs without sulfide segregation and with $Na_{8.0}$ lower than the global average were taken to estimate the Sn isotope composition of DMM, which yielded $\delta^{122/118}Sn_{BHVO\text{-}2}$ of 0.036 ± 0.087‰ ($\delta^{122/118}Sn_{3161a}$ of 0.367 ± 0.087‰) (2SD, $N = 12$).

Primary MORB magmas have MgO contents higher than 9 wt% (Niu, 2016). During MORB generation processes, olivine fractional crystallization and accumulation could result in a linear relationship between the logarithmic contents of incompatible elements like Ni and MgO (Fig. 13), which can be used to determine parental magma composition (Ma et al., 2022; Nebel et al., 2014). Our data on the relationship between MgO and Ni largely overlap that of Ma et al. (2022) and display no breakpoint (Fig. 13). Therefore, the MORB with the highest MgO content could be taken to approximate that of the primary melts, which yields $\delta^{122/118}Sn_{BHVO\text{-}2}$ of 0.017 ± 0.031‰ ($\delta^{122/118}Sn_{3161a}$ of 0.348 ± 0.031‰). These two approaches (based on the lowest $Na_{8.0}$ vs. based on the highest MgO content) give consistent results.

The formation and recycling of the oceanic crust are responsible for the differentiation/cooling of the Earth and the chemical heterogeneity of the mantle (Coogan, 2014; Hofmann, 1988; Stracke, 2021). The oceanic crust occupies 60% of Earth's surface and mainly consists of MORBs (White and Klein, 2014). The distribution of Sn isotope compositions versus $Na_{8.0}$ allows us to estimate the Sn isotope composition for the bulk oceanic crust. The average Na8.0 in the global mid-ocean

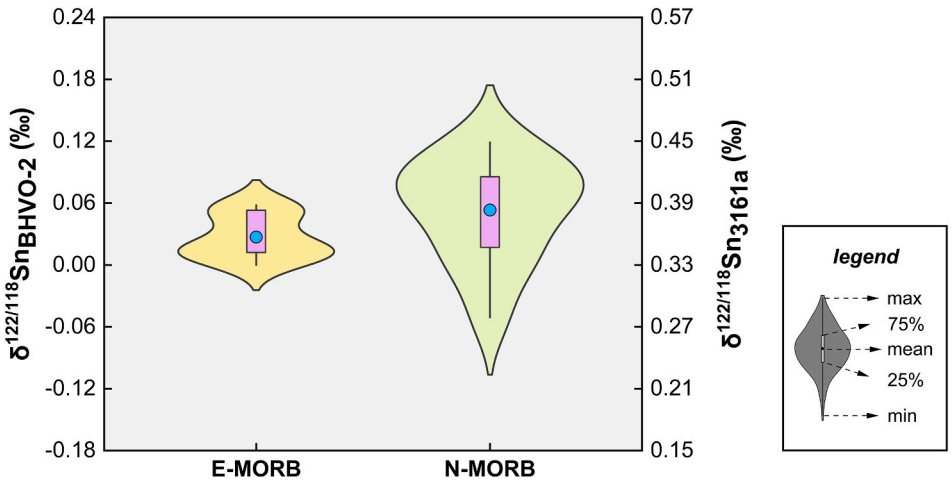

Fig. 12. Violin plot of the Sn isotope distribution for two groups of MORBs. The width of each curve corresponds with the approximate frequency of data points in each region. In the middle of each density curve is a small box plot, with the rectangle showing the ends of the first and third quartiles and the central dot the mean. The line following the rectangle shows the maximum and minimum values.

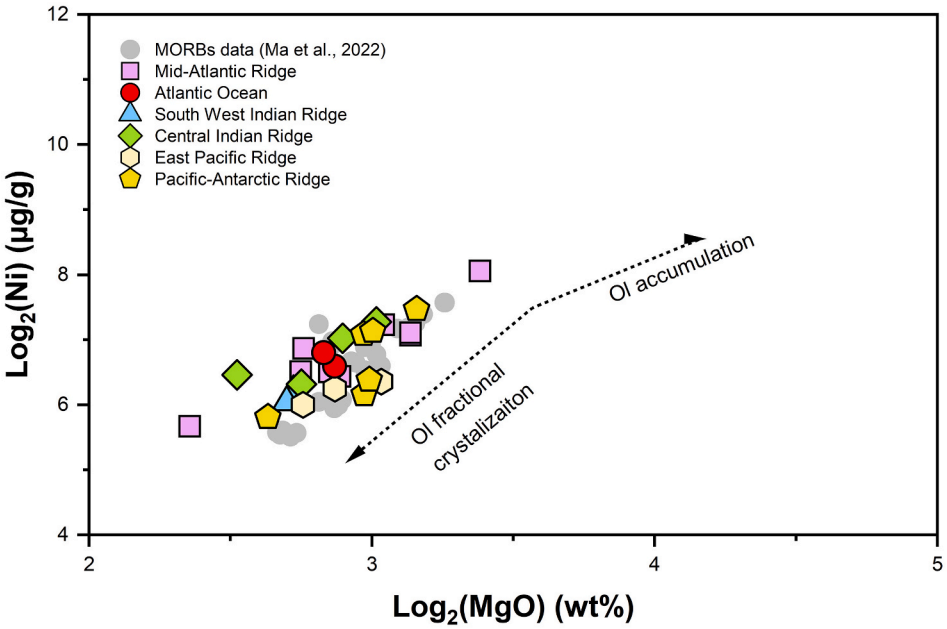

Fig. 13. Variations of Ni (μg/g) as a function of MgO (wt%) of MORB analyzed in this study. The trend of Ol crystallization and accumulation are modified from Ma et al. (2022b). The gray circles represent the published MORBs data from Ma et al. (2022).

ridge system covers a range of 1.75 to 3.75 wt% (White and Klein, 2014), in which 20 of our samples fall. The oceanic crust was estimated to have the average $\delta^{122/118}Sn_{BHVO\text{-}2}$ of 0.048 ± 0.085‰ ($\delta^{122/118}Sn_{3161a}$ of 0.379 ± 0.085‰) (2SD, $N = 20$) based on these samples.

5. Conclusions

The lack of faithful constraints on the Sn isotope signature of the Earth's mantle had hampered the assessment of planetary formation and differentiation using Sn isotopes. This study aims to characterize the Sn isotope signature of the mid-ocean ridge basalts and to evaluate the effect of various magmatic processes on Sn isotopic composition at mid-ocean ridges. A set of representative MORB samples spanning a wide range in chemical composition and localities have $\delta^{122/118}Sn_{BHVO\text{-}2}$ values that range from −0.051 ± 0.015‰ to 0.209 ± 0.016‰ ($\delta^{122/118}Sn_{3161a}$ from 0.280 ± 0.015 to 0.540 ± 0.016‰). The highest $\delta^{122/118}Sn$ value is measured from the sample with evidence of alteration. The magnitude of Sn isotope variability among the fresh MORBs is comparable, or only slightly greater than, the current analytical precision, and there is a lack of correlations between Sn isotope compositions with position, spreading rate, MgO content, and $Na_{8.0}$. Based on this, we infer that the MORB mantle source is homogeneous in terms of Sn isotopes. The best estimate of the $\delta^{122/118}Sn_{BHVO\text{-}2}$ for the Earth's depleted MORB mantle is 0.036 ± 0.087‰ ($\delta^{122/118}Sn_{3161a}$ of 0.367 ± 0.087‰) (2SD, $N = 12$).

Declaration of Competing Interest

The authors declare that they have no known competing financial interests or personal relationships that could have appeared to influence the work reported in this paper.

Data availability

Data will be made available on request.

Acknowledgment

We thank Maria Schönbächler, Ryan Mathur, and one anonymous reviewer for their reviews that led to improvements in the manuscript. We thank Dimitri Rigoussen and Pascale Louvat for their help in the lab and instrument. SJX is supported by a grant from the China Scholarship Council (File No. 202006190253) and the program A/B for Outstanding PhD candidate of Nanjing University. This study was supported by Frontiers Science Center for Critical Earth Material Cycling, Nanjing University (Grant Number: DLTD2103), China National Space Administration (Grant Number: D020205), and National Natural Science Foundation of China (Grant Number 41873004) to WL. This work was supported by the IPGP analytical platform PARI, Region Ile-de-France SESAME Grants no. 12015908, and DIM ACAV +, the ERC grant agreement No. 101001282 (METAL) (F.M.), the UnivEarthS Labex program (numbers: ANR-10-LABX-0023 and ANR-11-IDEX-0005-02) (F. M.).

Appendix A. Supplementary data

Supplementary data to this article can be found online at https://doi.org/10.1016/j.chemgeo.2023.121347.

References

Abdel Ghani, S.A., 2015. Trace metals in seawater, sediments and some fish species from Marsa Matrouh Beaches in North-Western Mediterranean coast, Egypt. Egyp. J. Aquat. Res. 41 (2), 145–154.
Adam, J., Green, T., 2006. Trace element partitioning between mica- and amphibole-bearing garnet lherzolite and hydrous basanitic melt: 1. Experimental results and the investigation of controls on partitioning behaviour. Contrib. Mineral. Petrol. 152, 1–17.
Amsellem, E., et al., 2018. The stable strontium isotopic composition of ocean island basalts, mid-ocean ridge basalts, and komatiites. Chem. Geol. 483, 595–602.
Anguelova, M., Fehr, M.A., Takazawa, E., Schönbächler, M., 2022. Titanium isotope heterogeneity in the Earth's mantle: a case study of the Horoman peridotite massif. Geochim. Cosmochim. Acta 335, 356–368.
Arevalo, R.J., McDonough, W.F., 2010. Chemical variations and regional diversity observed in MORB. Chem. Geol. 271, 70–85.
Badullovich, N., Moynier, F., Creech, J., Teng, F.Z., Sossi, P.A., 2017. Tin isotopic fractionation during igneous differentiation and Earth's mantle composition. Geochem. Perspect. Lett. 5, 24–28.
Barnes, J.J., et al., 2016. Early degassing of lunar urKREEP by crust-breaching impact(s). Earth Planet. Sci. Lett. 447, 84–94.
Berger, D., Figueiredo, E., Bruegmann, G., Pernicka, E., 2018. Tin isotope fractionation during experimental cassiterite smelting and its implication for tracing the tin sources of prehistoric metal artefacts. J. Archaeol. Sci. 92, 73–86.

Bezard, R., Fischer-Gödde, M., Hamelin, C., Brennecka, G.A., Kleine, T., 2016. The effects of magmatic processes and crustal recycling on the molybdenum stable isotopic composition of Mid-Ocean Ridge Basalts. Earth Planet. Sci. Lett. 453, 171–181.
Bienvenu, P., Bougault, H., Joron, J.L., Treuil, M., Dmitriev, L., 1990. MORB alteration: Rare-earth element/non-rare-earth hygromagmaphile element fractionation. Chem. Geol. 82, 1–14.
Borghini, G., et al., 2021. Enriched Hf Nd isotopic signature of veined pyroxenite-infiltrated peridotite as a possible source for E-MORB. Chem. Geol. 586, 120591.
Brandl, P.A., et al., 2012. Volcanism on the flanks of the East Pacific rise: Quantitative constraints on mantle heterogeneity and melting processes. Chem. Geol. 298-299, 41–56.
Bruegmann, G., Berger, D., Pernicka, E., 2017. Determination of the Tin Stable Isotopic Composition in Tin-bearing Metals and Minerals by MC-ICP-MS. Geostand. Geoanal. Res. 41, 437–448.
Buck, W.R., Poliakov, A.N.B., 1998. Abyssal hills formed by stretching oceanic lithosphere. Nature 392 (6673), 272–275.
Byerly, G., Sinton, J.M., 1980. Compositional trends in natural basaltic glasses from Deep Sea Drilling Project Holes 417D and 418A. Initial Rep. Deep Sea Drill. Proj. 51, 957–971.
Byrd, J.T., Andreae, M.O., 1982. Tin and Methyltin Species in Seawater: Concentrations and Fluxes. Science 218 (4572), 565–569.
Chauvel, C., Blichert-Toft, J., 2001. A hafnium isotope and trace element perspective on melting of the depleted mantle. Earth Planet. Sci. Lett. 190, 137–151.
Che, X.D., Linnen, R.L., Wang, R.C., Groat, L.A., Brand, A.A., 2013. Distribution of trace and rare earth elements in titanite from tungsten and molybdenum deposits in Yukon and British Columbia, Canada. Can. Mineral. 51 (3), 415–438.
Chen, M.-M., et al., 2014. Peridotite and pyroxenite xenoliths from Tarim, NW China: Evidences for melt depletion and mantle refertilization in the mantle source region of the Tarim flood basalt. Lithos 204, 97–111.
Chen, S., et al., 2019a. Molybdenum systematics of subducted crust record reactive fluid flow from underlying slab serpentine dehydration. Nat. Commun. 10 (1), 4773.
Chen, S., et al., 2019b. Iron isotope fractionation during mid-ocean ridge basalt (MORB) evolution: evidence from lavas on the East Pacific rise at 10°30′N and its implications. Geochim. Cosmochim. Acta 267, 227–239.
Chen, C., et al., 2020. Calcium isotopic compositions of oceanic crust at various spreading rates. Geochim. Cosmochim. Acta 278, 272–288.
Chen, S., et al., 2022. Molybdenum isotope systematics of lavas from the East Pacific rise: Constraints on the source of enriched mid-ocean ridge basalt. Earth Planet. Sci. Lett. 578, 177283.
Clog, M., Aubaud, C., Cartigny, P., Dosso, L., 2013. The hydrogen isotopic composition and water content of southern Pacific MORB: a reassessment of the D/H ratio of the depleted mantle reservoir. Earth Planet. Sci. Lett. 381, 156–165.
Coogan, L.A., 2014. 4.14 - the lower Oceanic Crust. In: Holland, H.D., Turekian, K.K. (Eds.), Treatise on Geochemistry (Second Edition). Elsevier, Oxford, pp. 497–541.
Cotta, A.J.B., Enzweiler, J., 2013. Determination of Cr, Cu, Ni, Sn, Sr and Zn Mass Fractions in Geochemical Reference Materials by Isotope Dilution ICP-MS. Geostand. Geoanal. Res. 37 (1), 35–50.
Creech, J.B., Moynier, F., 2019. Tin and zinc stable isotope characterisation of chondrites and implications for early Solar System evolution. Chem. Geol. 511, 81–90.
Creech, J.B., Moynier, F., Badullovich, N., 2017. Tin stable isotope analysis of geological materials by double-spike MC-ICPMS. Chem. Geol. 457, 61–67.
Creech, J.B., Moynier, F., Koeberl, C., 2019. Volatile loss under a diffusion-limited regime in tektites: evidence from tin stable isotopes. Chem. Geol. 528, 119279.
Creech, J.B., Paul, B., 2015. IsoSpike: improved Double-Spike Inversion Software. Geostand. Geoanal. Res. 39 (1), 7–15.
Day, J.M.D., Moynier, F., 2014. Evaporative fractionation of volatile stable isotopes and their bearing on the origin of the Moon. Phil. Trans. R. Soc. A 372 (2024), 20130259.
DeMets, C., Gordon, R.G., Argus, D.F., Stein, S., 1990. Current plate motions. Geophys. J. Int. 101 (2), 425–478.
DeMets, C., Gordon, R.G., Argus, D.F., Stein, S., 1994. Effect of recent revisions to the geomagnetic reversal time scale on estimates of current plate motions. Geophys. Res. Lett. 21 (20), 2191–2194.
Deng, Z., et al., 2020. Early oxidation of the martian crust triggered by impacts. Sci. Adv. 6, eabc4941.
Deng, Z., Moynier, F., Sossi, P.A., Chaussidon, M., 2018. Bridging the depleted MORB mantle and the continental crust using titanium isotopes. Geochem. Perspect. Lett. 9, 11–15.
Deng, Z., et al., 2019. Titanium isotopes as a tracer for the plume or island arc affinity of felsic rocks. Proc. Natl. Acad. Sci. 116 (4), 1132.
Dick, H.J.B., Lin, J., Schouten, H., 2003. An ultraslow-spreading class of ocean ridge. Nature 426 (6965), 405–412.
Donnelly, K.E., Goldstein, S.L., Langmuir, C.H., Spiegelman, M., 2004. Origin of enriched ocean ridge basalts and implications for mantle dynamics. Earth Planet. Sci. Lett. 226 (3–4), 347–366.
Elsasser, W.M., 1971. Sea-floor spreading as thermal convection. J. Geophys. Res. (1896–1977) 76 (5), 1101–1112.
Emmermann, R., Puchelt, H., 1980. Major and trace element chemistry of basalts from holes 417D and 418A, Deep Sea Drilling Project legs 51-53. Initial Rep. Deep Sea Drill. Proj. 51, 987–1000.
Estep, J., Reece, B., Christeson, G.L., Kardell, D.A., Carlson, R.L., 2021. 70 million years of seafloor spreading and magmatism in the South Atlantic. Earth Planet. Sci. Lett. 574, 17173.
Fan, J.-J., et al., 2020. High-precision molybdenum isotope analysis of low-Mo igneous rock samples by MC–ICP–MS. Chem. Geol. 545, 119648.
Gale, A., Dalton, C.A., Langmuir, C.H., Su, Y., Schilling, J.-G., 2013. The mean composition of ocean ridge basalts. Geochem. Geophys. Geosyst. 14 (3), 489–518.
Gargano, A., et al., 2022. The Zn, S, and Cl isotope compositions of mare basalts: implications for the effects of 1 eruption style and pressure on volatile element stable isotope fractionation on the Moon. Am. Mineral. https://doi.org/10.2138/am-2022-8290.
German, C.R., Seyfried, W.E., 2014. 8.7 - Hydrothermal Processes. In: Holland, H.D., Turekian, K.K. (Eds.), Treatise on Geochemistry. Elsevier, Oxford, pp. 191–233 (Second Edition).
Greaney, A.T., et al., 2017. The behavior of chalcophile elements during magmatic differentiation as observed in Kilauea Iki lava lake, Hawaii. Geochim. Cosmochim. Acta 210, 71–96.
Grindlay, N.R., Madsen, J.A., Rommevaux-Jestin, C., Sclater, J., 1998. A different pattern of ridge segmentation and mantle Bouguer gravity anomalies along the ultra-slow spreading Southwest Indian Ridge (15°30′E to 25°E). Earth Planet. Sci. Lett. 161 (1), 243–253.
Guo, P., et al., 2023. Low-degree melt metasomatic origin of heavy Fe isotope enrichment in the MORB mantle. Earth Planet. Sci. Lett. 601, 17892.
Hamelin, C., et al., 2011. Geochemical portray of the Pacific Ridge: New isotopic data and statistical techniques. Earth Planet. Sci. Lett. 302 (1–2), 154–162.
Hart, S.R., 1988. Heterogeneous mantle domains: signatures, genesis and mixing chronologies. Earth Planet. Sci. Lett. 90 (3), 273–296.
Hofmann, A.W., 1988. Chemical differentiation of the Earth: the relationship between mantle, continental crust, and oceanic crust. Earth Planet. Sci. Lett. 90 (3), 297–314.
Hofmann, A.W., 1997. Mantle geochemistry: the message from oceanic volcanism. Nature 385 (6613), 219–229.
Hu, Y., Teng, F.-Z., Zhang, H.-F., Xiao, Y., Su, B.-X., 2016. Metasomatism-induced mantle magnesium isotopic heterogeneity: evidence from pyroxenites. Geochim. Cosmochim. Acta 185, 88–111.
Huang, Y., Chubakov, V., Mantovani, F., Rudnick, R.L., McDonough, W.F., 2013. A reference Earth model for the heat-producing elements and associated geoneutrino flux. Geochem. Geophys. Geosyst. 14 (6), 2003–2029.
Huang, J., Liu, S.-A., Gao, Y., Xiao, Y., Chen, S., 2016. Copper and zinc isotope systematics of altered oceanic crust at IODP Site 1256 in the eastern equatorial Pacific. J. Geophys. Res. Solid Earth 121 (10), 7086–7100.
Humphris, S.E., Thompson, G., Schilling, J.-G., Kingsley, R.H., 1985. Petrological and geochemical variations along the Mid-Atlantic Ridge between 46°S and 32°S: Influence of the Tristan da Cunha mantle plume. Geochim. Cosmochim. Acta 49 (6), 1445–1464.
Inglis, E.C., et al., 2019. Isotopic fractionation of zirconium during magmatic differentiation and the stable isotope composition of the silicate Earth. Geochim. Cosmochim. Acta 250, 311–323.
Jenner, F.E., 2017. Cumulate causes for the low contents of sulfide-loving elements in the continental crust. Nat. Geosci. 10 (7), 524–529.
Jochum, K.P., Hofmann, A.W., Seufert, H.M., 1993. Tin in mantle-derived rocks: Constraints on Earth evolution. Geochim. Cosmochim. Acta 57, 3585–3595.
Jochum, K.P., Verma, S.P., 1996. Extreme enrichment of Sb, Tl and other trace elements in altered MORB. Chem. Geol. 130 (3), 289–299.
Jenner, F.E., O'Neill, H.S.C., 2012. Analysis of 60 elements in 616 ocean floor basaltic glasses. Geochem. Geophys. Geosyst. 13 (2), Q02005.
Jochum, K.P., et al., 2016. Reference Values following ISO guidelines for frequently Requested Rock Reference Materials. Geostand. Geoanal. Res. 40 (3), 333–350.
Kamenetsky, V.S., Eggins, S.M., 2012. Systematics of metals, metalloids, and volatiles in MORB melts: Effects of partial melting, crystal fractionation and degassing (a case study of Macquarie Island glasses). Chem. Geol. 302-303, 76–86.
Kang, J.-T., et al., 2017. Calcium isotopic fractionation in mantle peridotites by melting and metasomatism and ca isotope composition of the Bulk Silicate Earth. Earth Planet. Sci. Lett. 474, 128–137.
Kato, C., Moynier, F., 2017. Gallium isotopic evidence for extensive volatile loss from the Moon during its formation. Sci. Adv. 3 (7), e1700571.
Kato, C., Moynier, F., Valdes, M.C., Dhaliwal, J.K., Day, J.M.D., 2015. Extensive volatile loss during formation and differentiation of the Moon. Nat. Commun. 6 (1), 7617.
Kim, J., et al., 2017. Mantle heterogeneity in the source region of mid-ocean ridge basalts along the northern Central Indian Ridge (8°S-17°S). Geochem. Geophys. Geosyst. 18 (4), 1419–1434.
Klein, E.M., Langmuir, C.H., 1987. Global correlations of ocean ridge basalt chemistry with axial depth and crustal thickness. J. Geophys. Res. Solid Earth 92 (B8), 8089–8115.
Kubik, E., et al., 2021. Tracing Earth's volatile delivery with tin. J. Geophys. Res. Solid Earth 126 (10), e2021JB022026.
Labidi, J., Cartigny, P., Hamelin, C., Moreira, M., Dosso, L., 2014. Sulfur isotope budget (32S, 33S, 34S and 36S) in Pacific–Antarctic ridge basalts: A record of mantle source heterogeneity and hydrothermal sulfide assimilation. Geochim. Cosmochim. Acta 133, 47–67.
LaFemina, P.C., 2015. Plate Tectonics and Volcanism. Encycloped. Volcan. 65–92.
Lambart, S., et al., 2019. Highly heterogeneous depleted mantle recorded in the lower oceanic crust. Nat. Geosci. 12 (6), 482–486.
Le Roux, V., et al., 2007. The Lherz spinel lherzolite: Refertilized rather than pristine mantle. Earth Planet. Sci. Lett. 259 (3–4), 599–612.
Leroux, P., Shirey, S., Hauri, E., Perfit, M., Bender, J., 2006. The effects of variable sources, processes and contaminants on the composition of northern EPR MORB (8–10°N and 12–14°N): evidence from volatiles (H2O, CO2, S) and halogens (F, Cl). Earth Planet. Sci. Lett. 251 (3–4), 209–231.
Li, Y., Audétat, A., 2012. Partitioning of V, Mn, Co, Ni, Cu, Zn, As, Mo, Ag, Sn, Sb, W, Au, Pb, and Bi between sulfide phases and hydrous basanite melt at upper mantle conditions. Earth Planet. Sci. Lett. 355-356, 327–340.
Liu, H., et al., 2021b. Potassium isotopic composition of low-temperature altered oceanic crust and its impact on the global K cycle. Geochim. Cosmochim. Acta. 311, 59–73.

Liu, S.-A., Li, S.-G., 2019. Tracing the Deep Carbon Cycle using Metal Stable Isotopes: Opportunities and challenges. Engineering 5 (3), 448–457.
Liu, P., Mao, J., Lehmann, B., Weyer, S., Horn, I., Mathur, R., Wang, F., Zhou, Z., 2021a. Tin isotopes via fs-LA-MC-ICP-MS analysis record complex fluid evolution in single cassiterite crystals. Am. Mineral. 106, 1980–1986.
Ma, H., Xu, L.-J., Shen, J., Liu, S.-A., Li, S., 2022. Chromium isotope fractionation during magmatic processes: evidence from Mid-ocean ridge basalts. Geochim. Cosmochim. 327, 79–95.
Marchesi, C., et al., 2013. Mantle refertilization by melts of crustal-derived garnet pyroxenite: evidence from the Ronda peridotite massif, southern Spain. Earth Planet. Sci. Lett. 362, 66–75.
Marty, B., Zimmermann, L., 1999. Volatiles (he, C, N, Ar) in mid-ocean ridge basalts: Assesment of shallow-level fractionation and characterization of source composition. Geochim. Cosmochim. Acta 63 (21), 3619–3633.
Mason, A., Powell, W., Bankoff, H.A., Mathur, R., Price, M., Bulatović, A., Filipović, V., 2020. Provenance of tin in the late Bronze Age balkans based on probabilistic and spatial analysis of Sn isotopes. J. Archaeol. Sci. 122, 105181.
Mathur, R., et al., 2017. Preparation and measurement of cassiterite for Sn isotope analysis. Geostand. Geoanal. Res. 41 (4), 701–707.
McCubbin, F.M., et al., 2015. Magmatic volatiles (H, C, N, F, S, Cl) in the lunar mantle, crust, and regolith: Abundances, distributions, processes, and reservoirs†. Am. Mineral. 100 (8–9), 1668–1707.
Michael, P.J., Cornell, W.C., 1998. Influence of spreading rate and magma supply on crystallization and assimilation beneath mid-ocean ridges: evidence from chlorine and major element chemistry of mid-ocean ridge basalts. J. Geophys. Res. Solid Earth 103 (B8), 18325–18356.
Michely, L.T., Leitzke, F.P., Speelmanns, I.M., Fonseca, R.O.C., 2017. Competing effects of crystal chemistry and silicate melt composition on trace element behavior in magmatic systems: insights from crystal/silicate melt partitioning of the REE, HFSE, Sn, in, Ga, Ba, Pt and Rh. Contrib. Mineral. Petrol. 172 (6), 39.
Moynier, F., et al., 2021. The Mercury Isotopic Composition of Earth's Mantle and the use of Mass Independently Fractionated Hg to Test for Recycled Crust. Geophys. Res. Lett. 48 (17), 2021GL094301.
Nebel, O., Campbell, I.H., Sossi, P.A., Van Kranendonk, M.J., 2014. Hafnium and iron isotopes in early Archean komatiites record a plume-driven convection cycle in the Hadean Earth. Earth Planet. Sci. Lett. 397, 111–120.
Nielsen, S.G., et al., 2018. Barium isotope evidence for pervasive sediment recycling in the upper mantle. Sci. Adv. 4 (7), eaas8675.
Niu, Y., 2016. The meaning of global ocean ridge basalt major element compositions. J. Petrol. 57 (11−12), 2081–2103.
Niu, Y., Hékinian, R., 1997a. Basaltic liquids and harzburgitic residues in the Garrett Transform: a case study at fast-spreading ridges1. Earth Planet. Sci. Lett. 146 (1), 243–258.
Niu, Y., Hékinian, R., 1997b. Spreading-rate dependence of the extent of mantle melting beneath ocean ridges. Nature 385 (6614), 326–329.
Niu, Y., O'Hara, M.J., 2008. Global Correlations of Ocean Ridge Basalt Chemistry with Axial Depth: a New Perspective. J. Petrol. 49 (4), 633–664.
Pak, S.-J., et al., 2017. Widespread tectonic extension at the Central Indian Ridge between 8°S and 18°S. Gondwana Res. 45, 163–179.
Paniello, R.C., Day, J.M.D., Moynier, F., 2012. Zinc isotopic evidence for the origin of the Moon. Nature 490 (7420), 376–379.
Patten, C., Barnes, S.-J., Mathez, E.A., Jenner, F.E., 2013. Partition coefficients of chalcophile elements between sulfide and silicate melts and the early crystallization history of sulfide liquid: LA-ICP-MS analysis of MORB sulfide droplets. Chem. Geol. 358, 170–188.
Peach, C.L., Mathez, E.A., Keays, R.R., 1990. Sulfide melt-silicate melt distribution coefficients for noble metals and other chalcophile elements as deduced from MORB: Implications for partial melting. Geochim. Cosmochim. Acta 54 (12), 3379–3389.
Poitrasson, F., Delpech, G., Grégoire, M., 2013. On the iron isotope heterogeneity of lithospheric mantle xenoliths: implications for mantle metasomatism, the origin of basalts and the iron isotope composition of the Earth. Contrib. Mineral. Petrol. 165 (6), 1243–1258.
Polyakov, V.B., Mineev, S.D., Clayton, R.N., Hu, G., Mineev, K.S., 2005. Determination of tin equilibrium isotope fractionation factors from synchrotron radiation experiments. Geochim. Cosmochim. Acta 69 (23), 5531–5536.
Pringle, E.A., Moynier, F., 2017. Rubidium isotopic composition of the Earth, meteorites, and the Moon: evidence for the origin of volatile loss during planetary accretion. Earth Planet. Sci. Lett. 473, 62–70.
Pringle, E.A., et al., 2016. Silicon isotopes reveal recycled altered oceanic crust in the mantle sources of Ocean Island Basalts. Geochim. Cosmochim. Acta 189, 282–295.
Rea, D.K., 1977. Local axial migration and spreading rate variations, East Pacific rise, 31°S. Earth Planet. Sci. Lett. 34 (1), 78–84.
Roskosz, M., et al., 2020. Redox and structural controls on tin isotopic fractionations among magmas. Geochim. Cosmochim. Acta 268, 42–55.
Rouxel, O., Dobbek, N., Ludden, J., Fouquet, Y., 2003. Iron isotope fractionation during oceanic crust alteration. Chem. Geol. 202 (1–2), 155–182.
Rudnick, R.L., Gao, S., 2003. 3.01 - Composition of the Continental Crust. In: Holland, H. D., Turekian, K.K. (Eds.), Treatise on Geochemistry. Pergamon, Oxford, pp. 1–64.
Saccani, E., et al., 2022. Geochemistry of basaltic blueschists from the Deyader Metamorphic complex (Makran Accretionary Prism, SE Iran): new constraints for magma generation in the Makran sector of the Neo-Tethys. J. Asian Earth Sci. 228.
Sano, T., Yamashita, S., 2019. Evolution, hydrothermal assimilation, and ascent of magma inferred from volatile contents in MORB glasses: an example from thick lava pile at IODP Site 1256. Lithos 346–347, 105143.
Sato, H.D., 2004. Mineral compositions of MORB from the Australian Antarctic Discordance (AAD): implications for mantle source characteristics. In: Proceedings of the Ocean Drilling Program, Scientific Results.
Saunders, N.J., Barling, J., Harvey, J., Fitton, J.G., Halliday, A.N., 2022. Heterogeneous nickel isotope compositions of the terrestrial mantle – part 2: Mafic lithologies. Geochim. Cosmochim. Acta 317, 349–364.
Sauter, D., Patriat, P., Rommevaux-Jestin, C., Cannat, M., Briais, A., 2001. The Southwest Indian Ridge between 49°15′E and 57°E: focused accretion and magma redistribution. Earth Planet. Sci. Lett. 192 (3), 303–317.
Savage, P.S., et al., 2015. Copper isotope evidence for large-scale sulphide fractionation during Earth's differentiation. Geochem. Perspect. Lett. 53–64.
Schilling, J.G., 1973. Iceland Mantle Plume: Geochemical Study of Reykjanes Ridge. Nature 242 (5400), 565–571.
Schmidt, K., et al., 2011. Fluid elemental and stable isotope composition of the Nibelungen hydrothermal field (8°18′S, Mid-Atlantic Ridge): Constraints on fluid–rock interaction in heterogeneous lithosphere. Chem. Geol. 280 (1), 1–18.
Sharp, Z.D., Shearer, C.K., McKeegan, K.D., Barnes, J.D., Wang, Y.Q., 2010. The Chlorine Isotope Composition of the Moon and Implications for an Anhydrous Mantle, 329 (5995), pp. 1050–1053.
She, J.-X., et al., 2020. Sn isotope fractionation during volatilization of Sn(IV) chloride: Laboratory experiments and quantum mechanical calculations. Geochim. Cosmochim. Acta 269, 184–202.
She, J.-X., Li, W., An, S., Cai, Y., 2023. High-precision double-spike Sn isotope analysis of geological materials by MC-ICP-MS. J. Anal. At. Spectrom. 38 (1), 142–155.
Soderman, C.R., Shorttle, O., Matthews, S., Williams, H.M., 2022. Global trends in novel stable isotopes in basalts: Theory and observations. Geochim. Cosmochim. Acta 318, 388–414.
Staudigel, H., 2014. 4.16 - Chemical Fluxes from Hydrothermal Alteration of the Oceanic Crust. In: Holland, H.D., Turekian, K.K. (Eds.), Treatise on Geochemistry (Second Edition). Elsevier, Oxford, pp. 583–606.
Stracke, A., 2021. A process-oriented approach to mantle geochemistry. Chem. Geol. 579, 120350.
Sun, Z., et al., 2020. Sulfur abundance and heterogeneity in the MORB mantle estimated by copper partitioning and sulfur solubility modelling. Earth Planet. Sci. Lett. 538, 116169.
Sun, S., Li, J., 2015. Determination of Zr, Nb, Mo, Sn, Hf, Ta, and W in seawater by N-benzoyl-N-phenylhydroxylamine extraction chromatographic resin and inductively coupled plasma-mass spectrometry. Microchem. J. 119, 102–107.
Sun, S.S., McDonough, W.F., 1989. Chemical and isotopic systematics of oceanic basalts: implications for mantle composition and processes. Geol. Soc. Lond., Spec. Publ. 42 (1), 313–345.
Teng, F.-Z., Dauphas, N., Huang, S., Marty, B., 2013. Iron isotopic systematics of oceanic basalts. Geochim. Cosmochim. Acta 107, 12–26.
Tomascak, P.B., Langmuir, C.H., le Roux, P.J., Shirey, S.B., 2008. Lithium isotopes in global mid-ocean ridge basalts. Geochim. Cosmochim. Acta 72 (6), 1626–1637.
Tuller-Ross, B., et al., 2019. Potassium isotope systematics of oceanic basalts. Geochim. Cosmochim. Acta 259, 144–154.
Ulrich, M., Hémond, C., Nonnotte, P., Jochum, K.P., 2012. OIB/seamount recycling as a possible process for E-MORB genesis. Geochem. Geophys. Geosyst. 13 (6), Q0AC19.
Van Dover, C.L., et al., 2001. Biogeography and Ecological setting of Indian Ocean Hydrothermal Vents. Science 294 (5543), 818–823.
Vithana, M.V.P., Xu, M., Zhao, X., Zhang, M., Luo, Y., 2019. Geological and geophysical signatures of the East Pacific rise 8°–10°N. Solid Earth Sci. 4 (2), 66–83.
Wang, X., Amet, Q., Fitoussi, C., Bourdon, B., 2018. Tin isotope fractionation during magmatic processes and the isotope composition of the bulk silicate Earth. Geochim. Cosmochim. Acta 228, 320–335.
Wang, X., Fitoussi, C., Bourdon, B., Amet, Q., 2017. A new method of Sn purification and isotopic determination with a double-spike technique for geological and cosmochemical samples. J. Anal. At. Spectrom. 32, 1009–1019.
Wang, X., Fitoussi, C., Bourdon, B., Fegley, B., Charnoz, S., 2019a. Tin isotopes indicative of liquid–vapour equilibration and separation in the Moon-forming disk. Nat. Geosci. 12 (9), 707–711.
Wang, X., Fitoussi, C., Bourdon, B., Righter, K., Amet, Q., 2021a. The Sn isotope composition of chondrites: implications for volatile element depletion in the Solar System. Geochim. Cosmochim. Acta. 312, 139–157.
Wang, K., Jacobsen, S.B., 2016. Potassium isotopic evidence for a high-energy giant impact origin of the Moon. Nature 538 (7626), 487–490.
Wang, Z.Y., Luo, Z.Y., Zhang, L., Liu, J.J., Li, J., 2022. Sn Isotopic Values in ten Geological Reference Materials by Double-Spike MC-ICP-MS. Geostand. Geoanal. Res. 46 (3), 547–561.
Wang, D., Mathur, R., Powell, W., Godfrey, L., Zheng, Y., 2019b. Experimental evidence for fractionation of tin chlorides by redox and vapor mechanisms. Geochim. Cosmochim. Acta 250, 209–218.
Wang, T., et al., 2021b. Sn(II) chloride speciation and equilibrium Sn isotope fractionation under hydrothermal conditions: a first principles study. Geochim. Cosmochim. Acta 300, 25–43.
Waters, C.L., Sims, K.W.W., Perfit, M.R., Blichert-Toft, J., Blusztajn, J., 2011. Perspective on the Genesis of E-MORB from Chemical and Isotopic Heterogeneity at 9–10°N East Pacific rise. J. Petrol. 52 (3), 565–602.
Weis, D., Kieffer, B., Maerschalk, C., Pretorius, W., Barling, J., 2005. High-precision Pb-Sr-Nd-Hf isotopic characterization of USGS BHVO-1 and BHVO-2 reference materials. Geochem. Geophys. Geosyst. 6 (2), Q02002.
White, W.M., 1985. Sources of oceanic basalts: Radiogenic isotopic evidence. Geology 13 (2), 115–118.

White, W.M., Klein, E.M., 2014. 4.13 - Composition of the Oceanic Crust. In: Holland, H. D., Turekian, K.K. (Eds.), Treatise on Geochemistry, Second edition. Elsevier, Oxford, pp. 457–496.
Witt-Eickschen, G., Palme, H., O'Neill, H.S.C., Allen, C.M., 2009. The geochemistry of the volatile trace elements as, Cd, Ga, in and Sn in the Earth's mantle: New evidence from in situ analyses of mantle xenoliths. Geochim. Cosmochim. Acta 73 (6), 1755–1778.
Wood, B.J., Smythe, D.J., Harrison, T., 2019. The condensation temperatures of the elements: a reappraisal. Am. Mineral. 104 (6), 844–856.
Wu, F., et al., 2018. Vanadium isotope compositions of mid-ocean ridge lavas and altered oceanic crust. Earth Planet. Sci. Lett. 493, 128–139.
Yang, S., Humayun, M., Salters Vincent, J.M., 2020. Elemental constraints on the amount of recycled crust in the generation of mid-oceanic ridge basalts (MORBs). Sci. Adv. 6 (26), eaba2923.
Yao, J., Mathur, R., Powell, W., Lehmann, B., Tornos, F., Wilson, M., Ruiz, J., 2018. Sn-isotope fractionation as a record of hydrothermal redox reactions. Am. Mineral. 103, 1591–1598.
Yi, W., Halliday, A.N., Lee, D.-C., Christensen, J.N., 1995. Indium and tin in basalts, sulfides, and the mantle. Geochim. Cosmochim. Acta 59 (24), 5081–5090.
Zeng, Z., et al., 2021. Iron, copper, and zinc isotopic fractionation in seafloor basalts and hydrothermal sulfides. Mar. Geol. 436, 106491.
Zhang, H., et al., 2021. Tracing material contributions from Saint Helena plume to the South Mid-Atlantic ridge system. Earth Planet. Sci. Lett. 572, 117130.
Zhang, H.-F., Goldstein, S.L., Zhou, X.-H., Sun, M., Cai, Y., 2009. Comprehensive refertilization of lithospheric mantle beneath the North China Craton: further Os–Sr–Nd isotopic constraints. J. Geol. Soc. 166 (2), 249–259.
Zhang, Z., Hirschmann, M.M., 2016. Experimental Constraints on Mantle Sulfide Melting up to 8 GPa, 101(1), pp. 181–192.
Zhao, X.-M., Zhang, H.-F., Zhu, X.-K., Zhu, B., Cao, H.-H., 2015. Effects of melt percolation on iron isotopic variation in peridotites from Yangyuan, North China Craton. Chem. Geol. 401, 96–110.
Zhou, Z.-H., Mao, J.-W., Zhao, J.-Q., Gao, X., Weyer, S., Horn, I., Holtz, F., Sossi, P.A., Wang, D.-C., 2022. Tin isotopes as geochemical tracers of ore-forming processes with Sn mineralization. Am. Mineral. 107, 2111–2127.
Zindler, A., Hart, S., 1986. Chemical geodynamics. Annu. Rev. Earth Planet. Sci. 14, 493–571.